

1 Firing rate adaptation affords place 2 cell theta sweeps, phase precession 3 and procession

4 Tianhao Chu^{1†}, Zilong Ji^{1,2†}, Junfeng Zuo¹, Yuanyuan Mi³, Wen-hao Zhang⁴, Tiejun
5 Huang⁵, Daniel Bush⁶, Neil Burgess², Si Wu^{1‡}

*For correspondence:
siwu@pku.edu.cn (FMS)

[†]These authors contributed
equally to this work
[‡]Corresponding author

Present address: ⁵Department,
Institute, Country; [¶]Department,
Institute, Country

6 ¹School of Psychology and Cognitive Sciences, IDG/McGovern Institute for Brain
7 Research, Center of Quantitative Biology, Peking-Tsinghua Center for Life Sciences,
8 Academy for Advanced Interdisciplinary Studies, Peking University, China.; ²Institute of
9 Cognitive Neuroscience, University College London, UK.; ³Center for Neurointelligence,
10 School of Medicine, Chongqing University, China.; ⁴Lyda Hill Department of
11 Bioinformatics, O'Donnell Brain Institute, UT Southwestern Medical Center, USA.;
12 ⁵School of Computer Science, Peking University, China.; ⁶Department of Neuroscience,
13 Physiology and Pharmacology, University of College London, UK.

15 **Abstract** Hippocampal place cells in freely moving rodents display both theta phase precession
16 and procession, which is thought to play important roles in cognition, but the neural mechanism
17 for producing theta phase shift remains largely unknown. Here we show that firing rate
18 adaptation within a continuous attractor neural network causes the neural activity bump to
19 oscillate around the external input, resembling theta sweeps of decoded position during
20 locomotion. These forward and backward sweeps naturally account for theta phase precession
21 and procession of individual neurons, respectively. By tuning the adaptation strength, our model
22 explains the difference between “bimodal cells” showing interleaved phase precession and
23 procession, and “unimodal cells” in which phase precession predominates. Our model also
24 explains the constant cycling of theta sweeps along different arms in a T-maze environment, the
25 speed modulation of place cells’ firing frequency, and the continued phase shift after transient
26 silencing of the hippocampus. We hope that this study will aid an understanding of the neural
27 mechanism supporting theta phase coding in the brain.

29 Introduction

30 One of the strongest candidates for temporal coding of a cognitive variable by neural firing is the
31 ‘theta phase precession’ shown by hippocampal place cells. As an animal runs through the firing
32 field of a place cell, the cell fires at progressively earlier phases in successive cycles of the ongoing
33 LFP theta oscillation, so that firing phase correlates with distance traveled (*O’Keefe and Recce,*
34 *1993; Skaggs et al., 1996*) (see also (*Schmidt et al., 2009*)) (Fig. 1a&b). At the population level,
35 phase precession of individual cells gives rise to forward theta sequences once starting phases
36 are aligned across the population (*Feng et al., 2015*), where neurons representing successive lo-
37 cations along the trajectory of the animal display predictable firing sequences within individual
38 theta cycles (*Johnson and Redish, 2007*). These prospective sequential experiences (looking into
39 the future) are potentially useful for a range of cognitive faculties, e.g., planning, imagination, and
40 decision-making (*O’Keefe and Recce, 1993; Skaggs et al., 1996; Hassabis et al., 2007; Wikenheiser*

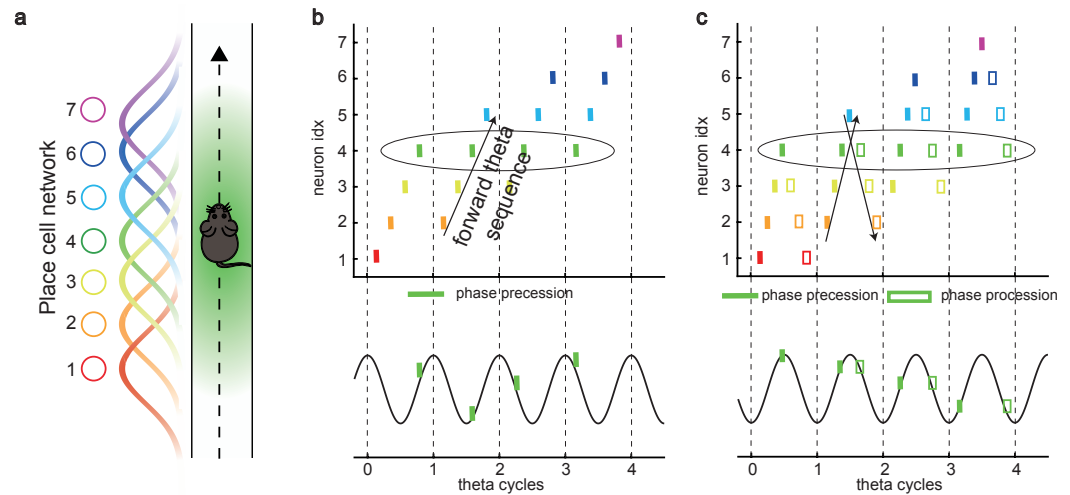


Figure 1. Theta sequence and theta phase shift of place cell firing. **a**, An illustration of an animal running on a linear track. A group of place cells each represented by a different color are aligned according to their firing fields on the linear track. **b**, An illustration of the forward theta sequences of the neuron population (upper panel), and the theta phase precession of the 4th place cell (represented by the green color, lower panel). **c**, An illustration of both forward and reverse theta sequences (upper panel), and the corresponding theta phase precession and procession of the 4th place cell (lower panel). The sinusoidal trace illustrates the theta rhythm of local field potential (LFP), with individual theta cycles separated by vertical dashed lines.

41 *and Redish, 2015; Kay et al., 2020*).

42 Besides prospective representation, flexible behaviors also require retrospective representa-
43 tion of sequential experiences (looking into the past). For instance, in goal-directed behaviors, it
44 is important to relate the reward information that might only occur at the end of a sequence of
45 events to preceding events in the sequence (*Foster et al., 2000; Foster and Wilson, 2006; Diba and*
46 *Buzsáki, 2007*). A recent experimental study (*Wang et al., 2020*) described retrospective sequences
47 during online behaviors (also indicated by (*Skaggs et al., 1996; Yamaguchi et al., 2002*)), namely, re-
48 verse theta sequences, interleaved with forward theta sequences in individual theta cycles (Fig. 1c).
49 Such retrospective sequences, together with the prospective sequences, may cooperate to estab-
50 lish higher-order associations in episodic memory (*Diba and Buzsáki, 2007; Jaramillo and Kempter,*
51 *2017; Pfeiffer, 2020*).

52 While a large number of computational models of phase precession and the associated for-
53 ward theta sequences have been proposed, e.g., the single cell oscillatory models (*O'Keefe and*
54 *Recce, 1993; Kamondi et al., 1998; Harris et al., 2002; Lengyel et al., 2003; Losonczy et al., 2010*)
55 and recurrent activity spreading models (*Tsodyks et al., 1996; Romani and Tsodyks, 2015*), the
56 underlying neural mechanism for interleaved forward- and reverse-ordered sequences remains
57 largely unclear. Do reverse theta sequences share the same underlying neural mechanism as for-
58 ward sequences, or do they reflect different mechanisms? If they do, what kind of neural architec-
59 ture can support the emergence of both kinds of theta phase shift? Furthermore, since forward
60 theta sequences are commonly seen, but reverse theta sequences are only seen in some circum-
61 stances (*Wang et al., 2020*), are they commensurate with forward theta sequences? If not, to what
62 degree are forward theta sequences more significant than the reverse ones?

63 To address these questions, we built a continuous attractor neural network (CANN) of the hip-
64 pocampal place cell population (*Amari, 1977; Tsodyks and Sejnowski, 1995; Samsonovich and Mc-*
65 *Naughton, 1997; Tsodyks, 1999*). The CANN conveys a map of the environment in its recurrent con-
66 nections that affords a single bump of activity on a topographically organized sheet of cells which
67 can move smoothly so as to represent the location of the animal as it moves in the environment.
68 Each neuron exhibits firing rate adaptation which destabilizes the bump attractor state. When the
69 adaptation is strong enough, the network bump can travel spontaneously in the attractor space,

70 which we term as the intrinsic mobility. Intriguingly, we show that, under competition between
 71 the intrinsic mobility and the extrinsic mobility caused by location-dependent sensory inputs, the
 72 network displays an oscillatory tracking state, in which the network bump sweeps back and forth
 73 around the external sensory input. This phenomenon naturally explains the theta sweeps found
 74 in the hippocampus (*Skaggs et al., 1996; Burgess et al., 1994; Foster and Wilson, 2007*), where the
 75 decoded position sweeps around the animal's physical position at theta frequency. More specifi-
 76 cally, phase precession occurs when the bump propagates forward while phase precession occurs
 77 when the network bump propagates backward. Moreover, we find that neurons can exhibit ei-
 78 ther only predominant phase precession (unimodal cells) when adaptation is relatively strong, or
 79 interleaved phase precession and procession (bimodal cells) when adaptation is relatively weak.

80 In addition to theta phase shift, our model also successfully explains the constant cycling of
 81 theta sweeps along different upcoming arms in a T-maze environment (*Kay et al., 2020*), and other
 82 phenomena related to phase precession of place cells (*Geisler et al., 2007; Zugaro et al., 2005*).
 83 We hope that this study facilitates our understanding of the neural mechanism underlying the
 84 rich dynamics of hippocampal neurons and lays the foundation for unveiling their computational
 85 functions.

86 Results

87 A network model of hippocampal place cells

88 To study the phase shift of hippocampal place cells, we focus on a one-dimensional (1D) continuous
 89 attractor neural network (CANN) (mimicking the animal moving on a linear track, see Fig. 2a), but
 90 generalization to the 2D case (mimicking the animal moving in a 2D arena) is straightforward (see
 91 Discussion for more details). Neurons in the 1D CANN can be viewed as place cells rearranged ac-
 92 cording to the locations of their firing fields on the linear track (measured during free exploration).
 93 The dynamics of the 1D CANN is written as

$$\tau \frac{dU(x, t)}{dt} = -U(x, t) + \rho \int_{-\infty}^{\infty} J(x, x') r(x', t) dx' - V(x, t) + I^{ext}(x, t), \quad (1)$$

$$r(x, t) = \frac{gU(x, t)^2}{1 + k\rho \int_{-\infty}^{\infty} U^2(x', t) dx'}, \quad (2)$$

94 Here $U(x, t)$ represents the presynaptic input to the neuron located at position x on the linear track,
 95 and $r(x, t)$ represents the corresponding firing rate constrained by global inhibition (*Hao et al.,*
 96 *2009*). τ is the time constant, ρ the neuron density, k the global inhibition strength, and g is the
 97 gain factor. The dynamics of $U(x, t)$ is determined by the leaky term $-U(x, t)$, the recurrent input
 98 from other neurons, the firing rate adaptation $-V(x, t)$, and the external input $I^{ext}(x, t)$. The recur-
 99 rent connection strength $J(x, x')$ between two neurons decays with their distance. For simplicity,
 100 we set $J(x, x')$ to be the Gaussian form, i.e., $J(x, x') = J_0/(2\pi a) \exp[-(x - x')^2/(2a^2)]$, with J_0 control-
 101 ling the connection strength and a the range of neuronal interaction. Such connectivity gives rise
 102 to a synaptic weight matrix with the property of translation invariance. Together with the global
 103 inhibition, the translation invariant weight matrix ensures that the network can hold a continuous
 104 family of stationary states (attractors) when no external input and adaptation exist (*Tsodyks and*
 105 *Sejnowski, 1995; Samsonovich and McNaughton, 1997; McNaughton et al., 2006; Wu et al., 2008*),
 106 where each attractor is a localized firing bump representing a single spatial location (Fig. 2b). These
 107 bump states are expressed as (see Methods. for the parameter settings and SI.2 for the detailed
 108 mathematical derivation):

$$\bar{r}(x, t) = A_r(t) \exp \left\{ -\frac{[x - z(t)]^2}{2a^2} \right\}, \quad (3)$$

109 where $A_r(t)$ denotes the bump height and $z(t)$ the bump center, i.e., the spatial location represented
 110 by the network. For convenience, we set the external input to be of the Gaussian form, which

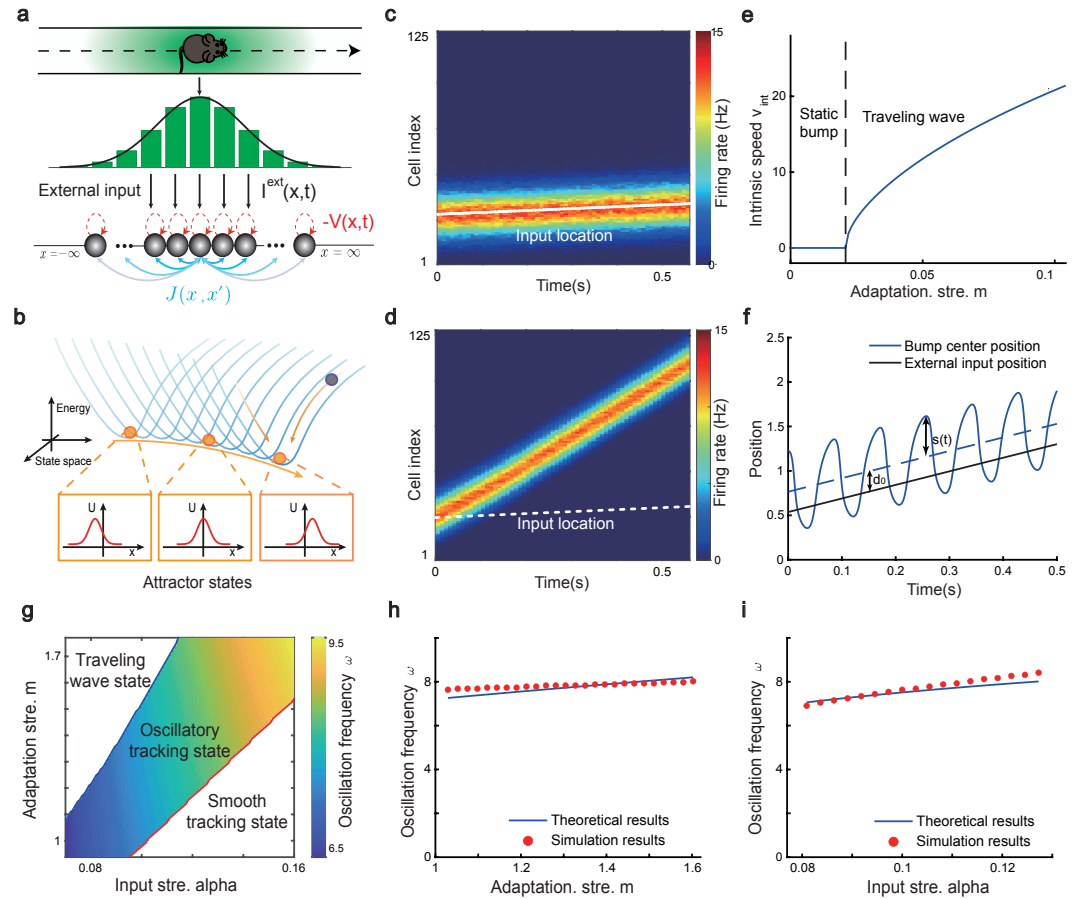


Figure 2. The network architecture and tracking dynamics. **a**, A 1D continuous attractor neural network formed by place cells. Neurons are aligned according to the locations of their firing fields on the linear track. The recurrent connection strength $J(x, x')$ (blue arrows) between two neurons decays with their distance on the linear track. Each neuron receives an adaptation current $-V(x, t)$ (red dashed arrows). The external input $I^{ext}(x, t)$, represented by a Gaussian-shaped bump, conveys location-dependent sensory inputs to the network. **b**, An illustration of the state space of the CANN. The CANN holds a family of bump attractors which form a continuous valley in the energy space. **c**, The smooth tracking state. The network bump (hot colors) smoothly tracks the external moving input (the white line). The red (blue) color represents high (low) firing rate. **d**, The travelling wave state when the CANN has strong firing rate adaptation. The network bump moves spontaneously with a speed much faster than the external moving input. **e**, The intrinsic speed of the travelling wave versus the adaptation strength. **f**, The oscillatory tracking state. The bump position sweeps around the external input (black line) with an offset d_0 . **g**, The phase diagram of the tracking dynamics with respect to the adaptation strength m and the external input strength α . The colored area shows the parameter regime for the oscillatory tracking state. Yellow (blue) color represents fast (slow) oscillation frequency. **h-i**, Simulated (red points) and theoretical (blue line) oscillation frequency as a function of the adaptation strength (**h**) or the external input strength (**i**).

111 is written as $I^{ext}(x, t) = \alpha \exp[-(x - v_{ext}t)^2/(4a^2)]$, with v_{ext} representing the moving speed and α
112 controlling the external input strength. Such external moving input represents location-dependent
113 sensory inputs (i.e., corresponding to the animal's physical location) which might be conveyed via
114 the entorhinal-hippocampal or subcortical pathways (*Van Strien et al., 2009*). The term $-V(x, t)$
115 represents the firing rate adaptation (*Alonso and Klink, 1993; Fuhrmann et al., 2002; Benda and*
116 *Herz, 2003*), whose dynamics is written as

$$\tau_v \frac{dV(x, t)}{dt} = -V(x, t) + mU(x, t), \quad (4)$$

117 where m controls the adaptation strength, and τ_v is the time constant. The condition $\tau_v \gg \tau$ holds,
118 implying that the firing rate adaptation is a much slower process compared to neuronal firing. In ef-
119 fect, the firing rate adaptation increases with the neuronal activity and contributes to destabilizing
120 the active bump state, which induce rich dynamics of the network (see below).

121 **Oscillatory tracking of the network**

122 Overall, the bump motion in the network is determined by two competing factors, i.e., the external
123 input and the adaptation. The interplay between these two factors leads to the network exhibiting
124 oscillatory tracking in an appropriate parameter regime. To elucidate the underlying mechanism
125 clearly, we explore the effects of the external input and the adaptation on bump motion separately.
126 First, when firing rate adaptation does not exist in the network ($m = 0$), the bump tracks the external
127 moving input smoothly (see Fig. 2c). We refer to this as the **"smooth tracking state"**, where the
128 internal location represented in the hippocampus (the bump position) is continuously tracking the
129 animal's physical location (the external input location). This smooth tracking property of CANNs
130 has been widely used to model spatial navigation in the hippocampus (*Tsodyks and Sejnowski,*
131 *1995; Samsonovich and McNaughton, 1997; McNaughton et al., 2006; Battaglia and Treves, 1998*).
132 Second, when the external drive does not exist in the network ($\alpha = 0$) and the adaptation strength
133 m exceeds a threshold ($m > \tau/\tau_v$), the bump moves spontaneously with a speed calculated as
134 $v_{int} = (2a/\tau_v) \sqrt{m\tau_v/\tau - \sqrt{m\tau_v/\tau}}$ (see Fig. 2d&e and Methods. for more details). We refer to this as
135 the **"travelling wave state"**, where the internal representation of location in the hippocampus is
136 sequentially reactivated without external drive, resembling replay-like dynamics during a quiescent
137 state (see Discussion for more details). This intrinsic mobility of the bump dynamics can be intu-
138 itively understood as follows. Neurons around the bump center have the highest firing rates and
139 hence receive the strongest adaptation. Such strong adaptation destabilizes the bump stability at
140 the current location, and hence pushes the bump away. After moving to a new location, the bump
141 will be continuously pushed away by the firing rate adaptation at the new location. As a result, the
142 bump keeps moving on the linear track. Similar mechanisms have been applied to explain mental
143 exploration (*Hopfield, 2010*), preplay during sharp wave-ripple events in the hippocampus (*Azizi*
144 *et al., 2013*), and the free memory recall phenomenon in the brain (*Dong et al., 2021*).

145 When both the external input and adaptation are applied to the CANN, the interplay between
146 the extrinsic mobility (caused by the external input) and the intrinsic mobility (caused by the adap-
147 tation) will induce three different dynamical behaviors of the network (see **video 1** for demonstra-
148 tion), i.e., 1) when m is small and α is large, the network displays the smooth tracking state; 2) when
149 m is large and α is small, the network displays the travelling wave state; 3) when both m and α have
150 moderate values, the network bump displays an interesting state, called the **"oscillatory tracking**
151 **state"**, where the bump tracks the external moving input in an oscillatory fashion (Fig. 2f&g). In-
152 tuitively, the mechanism for oscillatory tracking can be understood as follows. Due to the intrinsic
153 mobility of the network, the bump tends to move at its own intrinsic speed (which is faster than the
154 external moving input, see Fig. 2d), i.e., the bump tries to escape from the external input. However,
155 due to the strong locking effect of the external input, the bump can not run too far away from the
156 location input, but instead, is attracted back to the location input. Once the bump returns, it will
157 keep moving in the opposite direction of the external input until it is pulled back by the external

158 input again. Over time, the bump will sweep back and forth around the external moving input,
159 displaying the oscillatory tracking behavior.

160 Our study shows that during oscillatory tracking, the bump shape is roughly unchanged (see
161 Sec. for the condition of shape variability), and the bump oscillation can be well represented as
162 the bump center sweeping around the external input location. The dynamics of the bump center
163 can be approximated as a propagating sinusoidal wave (Fig. 2f), i.e.,

$$z(t) = c_0 \sin(\omega t) + d_0 + v_{ext}t = s(t) + v_{ext}t, \quad (5)$$

164 where $z(t)$ is the bump center at time t (see Eq. 3). $s(t)$ denotes the displacement between the bump
165 center and the external input, which oscillates at the frequency ω with the amplitude $c_0 > 0$ and a
166 constant offset $d_0 > 0$ (see Methods. for the values of these parameters and SI.3 for the detailed
167 derivation). When the firing rate adaptation is relatively small, the bump oscillation frequency can
168 be analytically solved to be (see also Fig.S1):

$$\omega = \sqrt{\frac{2\sqrt{\pi}\alpha ak(1+m)}{\tau\tau_v(J_0 + 2\sqrt{\pi}ak\alpha)}}. \quad (6)$$

169 We see that the bump oscillation frequency ω increases sublinearly with the external input strength
170 α and the adaptation strength m (Fig. 2h&i). By setting the parameters appropriately, the bump can
171 oscillate in the theta band (6-10 Hz), thus approximating the experimentally observed theta sweeps
172 (see below). Notably, LFP theta is not explicitly modelled in the network. However, since theta
173 sweeps are bounded by individual LFP theta cycles in experiments, they share the same oscillation
174 frequency as LFP theta. For convenience, we will frequently use LFP theta below and study firing
175 phase shift in individual oscillation cycles.

176 **Oscillatory tracking accounts for both theta phase precession and procession of** 177 **hippocampal place cells**

178 In our model, the bump center and external input represent the decoded and physical positions of
179 the animal, respectively, thus the oscillatory tracking of the bump around the external input natu-
180 rally gives rise to the forward and backward theta sweeps observed empirically (Fig. 3a&b) (*Wang*
181 *et al., 2020*). Here we show that oscillatory tracking of the bump accounts for the theta phase
182 precession and procession of place cell firing.

183 Without loss of generality, we select the neuron at location $x = 0$ as the probe neuron and ex-
184 amine how its firing phase changes as the external input traverses its firing field (Fig. 3c). In the
185 absence of explicitly simulated spike times, the firing phase of a neuron in each theta cycle is mea-
186 sured by the moment when the neuron reaches the peak firing rate (see Methods. for modeling
187 spike times in the CANN). Based on Eqs. 3 & 5, the firing rate of the probe neuron, denoted as $r_0(t)$,
188 is expressed as

$$r_0(t) = A_r(t) \exp\left[-\frac{[0 - z(t)]^2}{2a^2}\right] = A_r(t) \exp\left[-\frac{(v_{ext}t + c_0 \sin \omega t + d_0)^2}{2a^2}\right] \equiv A_r(t) \exp\left[-\frac{h(t)^2}{2a^2}\right], \quad (7)$$

189 where $A_r(t)$ is the bump height, and $h(t)$ is an oscillatory moving term denoting the displacement
190 between the bump center and the location of the probe neuron. It is composed of a moving signal
191 $v_{ext}t$ and an oscillatory signal $c_0 \sin \omega t + d_0$, with c_0 the oscillation amplitude, ω the frequency and d_0
192 an oscillation offset constant. It can be seen that the firing rate of the probe neuron is determined
193 by two factors, $A_r(t)$ and $h(t)$. To simplify the analysis below, we assume that the bump height $A_r(t)$
194 remains unchanged during bump oscillations (for the case of time-varying bump height, see Sec.).
195 Thus, the firing rate only depends on $h(t)$, which is further determined by two time-varying terms,
196 the oscillation term $c_0 \sin \omega t$ and the location of the external input $v_{ext}t$. The first term contributes

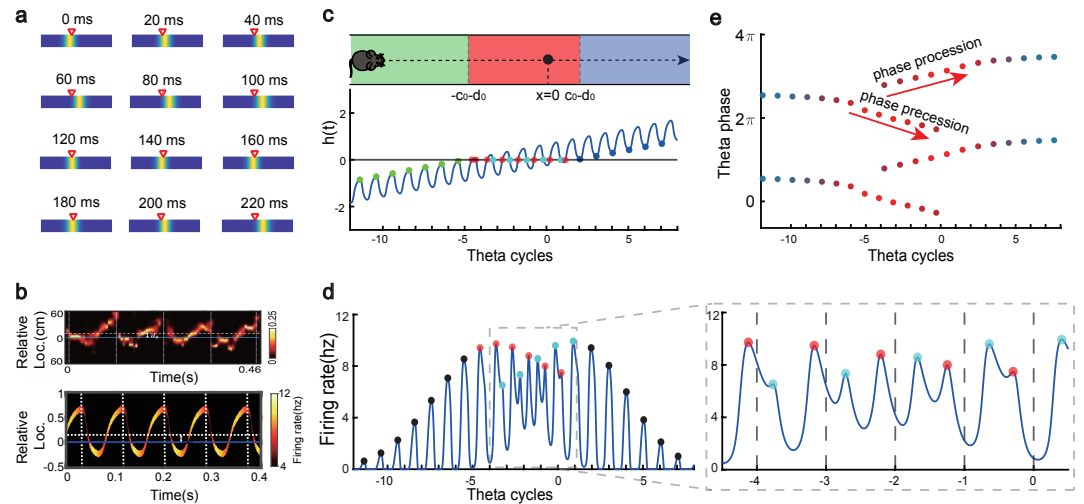


Figure 3. Oscillatory tracking accounts for theta sweeps and theta phase shift. **a**, Snapshots of the bump oscillation along the linear track in one theta cycle (0 ms - 140 ms). Red triangles indicate the location of the external moving input. **b**, Decoded relative positions based on place cell population activities. Upper panel: experimental data, adapted from *Wang et al. (2020)*. Lower panel: the relative locations of the bump center (shown by the 10 most active neurons at each timestamp) with respect to the location of the external input (horizontal line) in five theta cycles. **c**, Upper panel: the process of the animal running through the firing field of the probe neuron (large black dot) is divided into three stages: the entry stage (green), the phase shift stage (red) and the departure stage (blue). Lower panel: the displacement between the bump center and the probe neuron as the animal runs through the firing field. The horizontal line represents the location of the firing field, which is $x = 0$. **d**, The firing rates of the probe neuron as the animal runs through the firing field. Colored points indicate firing peaks. The trace of the firing rate in the phase shift stage (the dashed box) is enlarged in the sub-figure on the right hand-side, which exhibits both phase precession (red points) and procession (blue points) in successive theta cycles. **e**, The firing phase shift of the probe neuron in successive theta cycles. Red points progress to earlier phases from $\pi/2$ to $-\pi/2$ and blues points progress to later phases from $\pi/2$ to $3\pi/2$.

197 to firing rate oscillations of the probe neuron, and the second term contributes to the envelope
 198 of neuronal oscillations exhibiting a waxing-and-waning profile over time, as the external input
 199 traverses the firing field (the absolute value $|v_{ext}|$ first decreases and then increases; see Fig. 3d,
 200 also **video 2**). Such a waxing-and-waning profile agrees well with the experimental data (*Skaggs*
 201 *et al., 1996*). In each LFP theta cycle, the peak firing rate of the probe neuron is achieved when
 202 $|h(t)|$ reaches a local minima (Fig. 3c&d). We differentiate three stages as the external input passes
 203 through the probe neuron (i.e., the animal travels through the place field of the probe neuron), i.e.,

- 204 • **the entry stage.** As the external input enters the firing field of the probe neuron (moving
 205 from left to right), $h(t) < 0$ always holds (Fig. 3c). In this case, the peak firing rate of the
 206 probe neuron in each oscillatory cycle is achieved when $h(t)$ reaches the maximum (i.e., $|h(t)|$
 207 reaches the minimum). This corresponds to $c_0 \sin \omega t = c_0$, i.e., $\omega t = \pi/2$ (Fig. 3e). This means
 208 that the firing phase of the probe neuron at the entry stage is constant, which agrees with
 209 experimental observations (*O'Keefe and Recce, 1993; Skaggs et al., 1996*).
- 210 • **the phase shift stage.** As the external input moves into the centre of the firing field, $h(t) = 0$
 211 can be achieved in each oscillatory cycle (Fig. 3c). Notably, it is achieved twice in each cycle,
 212 once as the bump sweeps over the probe neuron in the forward direction and the other as
 213 the bump sweeps over the probe neuron in the backward direction. Therefore, there are
 214 two firing peaks in each bump oscillation cycle (Fig. 3d), which are expressed as (by solving
 215 $v_{ext}t + c_0 \sin \omega t + d_0 = 0$):

$$\phi_f = -\arcsin \left[\frac{d_0 + v_{ext}t_f}{c_0} \right], \quad \phi_b = \pi + \arcsin \left[\frac{d_0 + v_{ext}t_b}{c_0} \right], \quad (8)$$

216 where t_f and t_b denote the moments of peak firing in the forward and backward sweeps,

217 respectively, and ϕ_f and ϕ_b the corresponding firing phases of the probe neuron. As the
218 external input travels from $(-c_0 - d_0)$ to $(c_0 - d_0)$, the firing phase ϕ_f in the forward sweep
219 decreases from $\pi/2$ to $-\pi/2$, while the firing phase ϕ_r in the backward sweep increases from
220 $\pi/2$ to $3\pi/2$ (Fig. 3e). These give rise to the phase precession and procession phenomena,
221 respectively, agreeing well with experimental observations (Skaggs et al., 1996; Wang et al.,
222 2020; Yamaguchi et al., 2002).

223 • **the departure stage.** As the external input leaves the firing field, $h(t) > 0$ always holds
224 (Fig. 3c), and the peak firing rate of the probe neuron is achieved when $h(t)$ reaches its mini-
225 mum in each oscillatory cycle, i.e., $c_0 \sin(\omega t) = -c_0$ with $\omega t = \pi/2$ (Fig. 3e). Therefore, the firing
226 phase of the probe neuron is also constant during the departure stage

227 In summary, oscillatory tracking of the CANN well explains the firing phase shift of place cells
228 when the animal traverses their firing fields. Specifically, when the animal enters the place field,
229 the firing phase of the neuron remains constant, i.e., no phase shift occurs, which agrees with ex-
230 perimental observations (O'Keefe and Recce, 1993; Skaggs et al., 1996). As the animal approaches
231 the centre of the place field, the firing phase of the neuron starts to shift in two streams, one to ear-
232 lier phases during the forward sweeps and the other to later phases during the backward sweeps.
233 Finally, when the animal leaves the place field, the firing phase of the neuron stops shifting and
234 remains constant. Over the whole process, the firing phase of a place cell is shifted by 180 degrees,
235 which agrees with experimental observations (O'Keefe and Recce, 1993; Skaggs et al., 1996).

236 **Different adaptation strengths account for bimodal and unimodal cells**

237 The results above show that during oscillatory tracking, a place cell exhibits both significant phase
238 precession and procession, which are associated with two firing peaks in a theta cycle. These
239 neurons have been described as bimodal cells (Wang et al., 2020) (Fig. 4a). Conversely, previous
240 experiments have primarily focused on the phase precession of place cell firing, while tending
241 to ignore phase procession, which is a relatively weaker phenomenon (O'Keefe and Recce, 1993;
242 Skaggs et al., 1996). Place cells with negligible phase procession have been described as unimodal
243 cells (Fig. 4b).

244 Here, we show that by adjusting a single parameter in the model, i.e., the adaptation strength
245 m , neurons in the CANN can exhibit either interleaved phase precession and procession (bimodal
246 cells) or predominant phase precession (unimodal cells). To understand this, we first recall that
247 the firing rate adaptation is a much slower process compared to neural firing and its timescale is
248 in the same order as the LFP theta (i.e., $\tau_v = 100$ ms while $\tau = 5$ ms). This implies that when the
249 bump sweeps over a neuron, the delayed adaptation it generates will suppress the bump height
250 as it sweeps back to the same location. Furthermore, since the oscillatory tracking always begins
251 with a forward sweep (as the initial sweep is triggered by the external input moving in the same di-
252 rection), the suppression effects are asymmetric, that is, forward sweeps always strongly suppress
253 backward sweeps. On the contrary, the opposite effect is much smaller, since neuronal activities in
254 backward sweeps have already been suppressed, and they can only generate weak adaptation. Be-
255 cause of this asymmetric suppression, the bump height in the forward sweep is always higher than
256 that in the backward sweep (see Fig. 4c and Fig.S2a). When the adaptation strength m is small, the
257 suppression effect is not significant, and the attenuation of the bump height during the backward
258 sweep is small (Fig. 4d). In such case, the firing behavior of a place cell is similar to the situation as
259 the bump height remains unchanged as analyzed in Sec. , i.e., the neuron can generate two firing
260 peaks in a theta cycle at the phase shift stage, manifesting the property of a bimodal cell of having
261 both significant phase precession and procession (Fig. 4e&g and **video 2**). When the adaptation
262 strength m is large, the bump height in the backward sweep attenuates dramatically (see Fig. 4c&d
263 and the video demonstration). As a result, the firing peak of a place cell in the backward sweep
264 becomes nearly invisible at the phase shift stage, and the neuron exhibits only predominant phase
265 precession, manifesting the property of a unimodal cell (Fig. 4f&h and **video 3**).

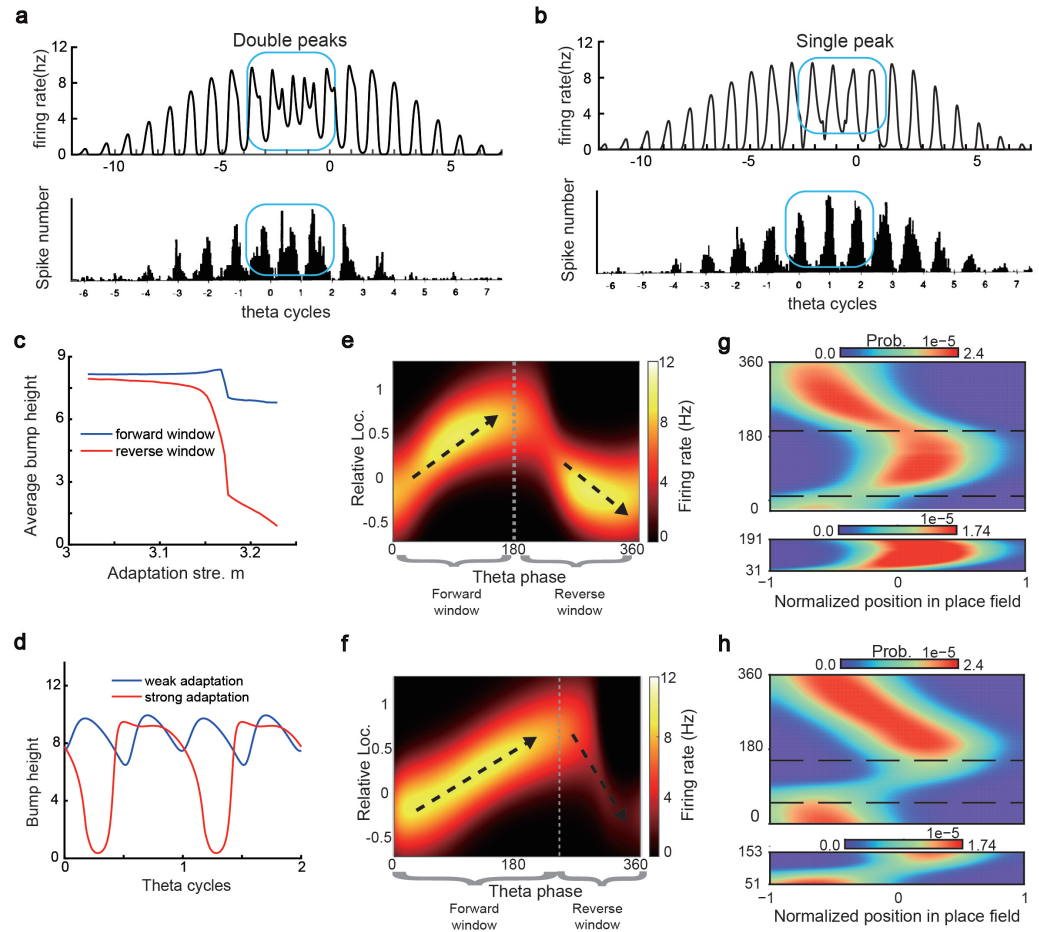


Figure 4. Different adaptation strengths account for the emergence of bimodal and unimodal cells. **a**, The firing rate trace of a typical bimodal cell in our model (upper panel) and the experiment data (lower panel, adapted from (Skaggs et al., 1996)). Blue boxes mark the phase shift stage. Note that there are two peaks in each theta cycle. **b**, The firing rate trace of a typical unimodal cell. Note that there is only one firing peak in each theta cycle. **c**, The averaged bump heights in the forward (blue curve) and backward windows (red curve) as a function of the adaptation strength m . **d**, Variation of the bump height when the adaptation strength is relatively small (blue line) or large (red line). **e-f**, Relative location of the bump center in a theta cycle when adaptation strength is relatively small (**e**) or large (**f**). Dashed line separate the forward and backward windows. **g-h**, Theta phase as a function of the normalized position of the animal in place field, averaged over all bimodal cells (**g**) or over all unimodal cells (**h**). -1 indicates that the animal just enters the place field, and 1 represents that the animal is about to leave the place field. Dashed lines separate the forward and backward windows. The lower panels in both **g** and **h** present the rescaled colormaps only in the backward window.

266 In summary, different adaptation strengths explain the emergence of bimodal and unimodal
267 cells. In fact, there is no sharp separation between bimodal and unimodal cells. As the firing rate
268 adaptation gets stronger, the network bump is more attenuated during the backwards sweep, and
269 cells with the bimodal firing property will gradually behave more like those with the unimodal fir-
270 ing property (see Fig.S2b). Moreover, our model confirms that even though phase procession is
271 weak, it still exist in unimodal cells (Fig. 4h lower panel), which has been reported in previous stud-
272 ies (*Wang et al., 2020; Yamaguchi et al., 2002*). This implies that phase procession is not a character-
273 istic feature of bimodal cells, but instead, is likely a common feature of hippocampal activity, with
274 a strength controlled by adaptation. Furthermore, the experimental data (*Fernández-Ruiz et al.,*
275 *2017*) has indicated that there is a laminar difference between unimodal cells and bimodal cells,
276 with bimodal cells correlating more with the firing patterns of deep CA1 neurons and unimodal
277 cells with the firing patterns of superficial CA1 neurons. Our model suggests that this difference
278 may come from the different adaptation strengths in the two layers.

279 **Constant cycling of multiple future scenarios in a T-maze environment**

280 We have shown that our model can reproduce the forward and backward theta sweeps of decoded
281 position when the animal runs on a linear track. It is noteworthy that there is only a single hypo-
282 theoretical future scenario in the linear track environment, i.e, ahead of the animal's position, and
283 hence place cells firing phase can only encode future positions in one direction. However, flexible
284 behaviors requires the animal encoding multiple hypothetical future scenarios in a quick and con-
285 stant manner, e.g., during decision-making and planning in complex environments (*Johnson and*
286 *Redish, 2007; Wikenheiser and Redish, 2015*). One recent study (*Kay et al., 2020*) showed constant
287 cycling of theta sweeps in a T-maze environment (Fig. 5a), that is, as the animal approaches the
288 choice point, the decoded position from hippocampal activity propagates down one of the two
289 arms alternatively in successive LFP theta cycles. To reproduce this phenomenon, we change the
290 structure of the CANN from a linear track shape to a T-maze shape where the neurons are aligned
291 according to the location of their firing fields in the T-maze environment. Neurons are connected
292 with a strength proportional to the Euclidean distance between their firing fields on the T-maze
293 and the parameters are set such that the network is in the oscillatory tracking state (see details in
294 Methods.). Mimicking the experimental protocol, we let the external input (the artificial animal)
295 move from the end of the center arm to the choice point. At the beginning, when the external
296 input is far away from the choice point, the network bump sweeps back and forth along the center
297 arm, similar to the situation on the linear track. As the external input approaches the choice point,
298 the network bump starts to sweep onto left and right arms alternatively in successive theta cycles
299 (Fig. 5b and **video 4**). The underlying mechanism is straightforward. Suppose that the bump first
300 sweeps to the left arm from the current location, it will sweep back to the current location first due
301 to the attraction of the external input. Then in the next round, the bump will sweep to the right
302 arm, since the neurons on the left arm are suppressed due to adaptation. This cycling process
303 repeats constantly between the two upcoming arms before the external input enters one of the
304 two arms (i.e, before the decision is made). At the single cell level, this bump cycling phenomenon
305 gives rise to the "cycle skipping" effect (*Kay et al., 2020; Deshmukh et al., 2010; Brandon et al.,*
306 *2013*), where a neuron whose place field is on one of the two arms fires on every other LFP theta
307 cycle before the decision is made (Fig. 5c left panel and Fig. 5d upper panel). For example, a pair of
308 cells with firing fields on each of the two arms will fire in regular alternation on every other theta
309 cycle (Fig. 5c right panel and Fig. 5d lower panel). These cell-level firing patterns agree well the
310 experimental observations (*Kay et al., 2020*).

311 In summary, our model, extended to a T-maze structure, explains the constant cycling of two
312 possible future scenarios in a T-maze environment. The underlying mechanism relies on delayed
313 adaptation, which alternately causes neurons on one arm to be more suppressed than those on
314 the other arm. Such high-speed cycling may contribute to the quick and continuous sampling
315 among multiple future scenarios in real-world decision-making and planning (see Discussion for

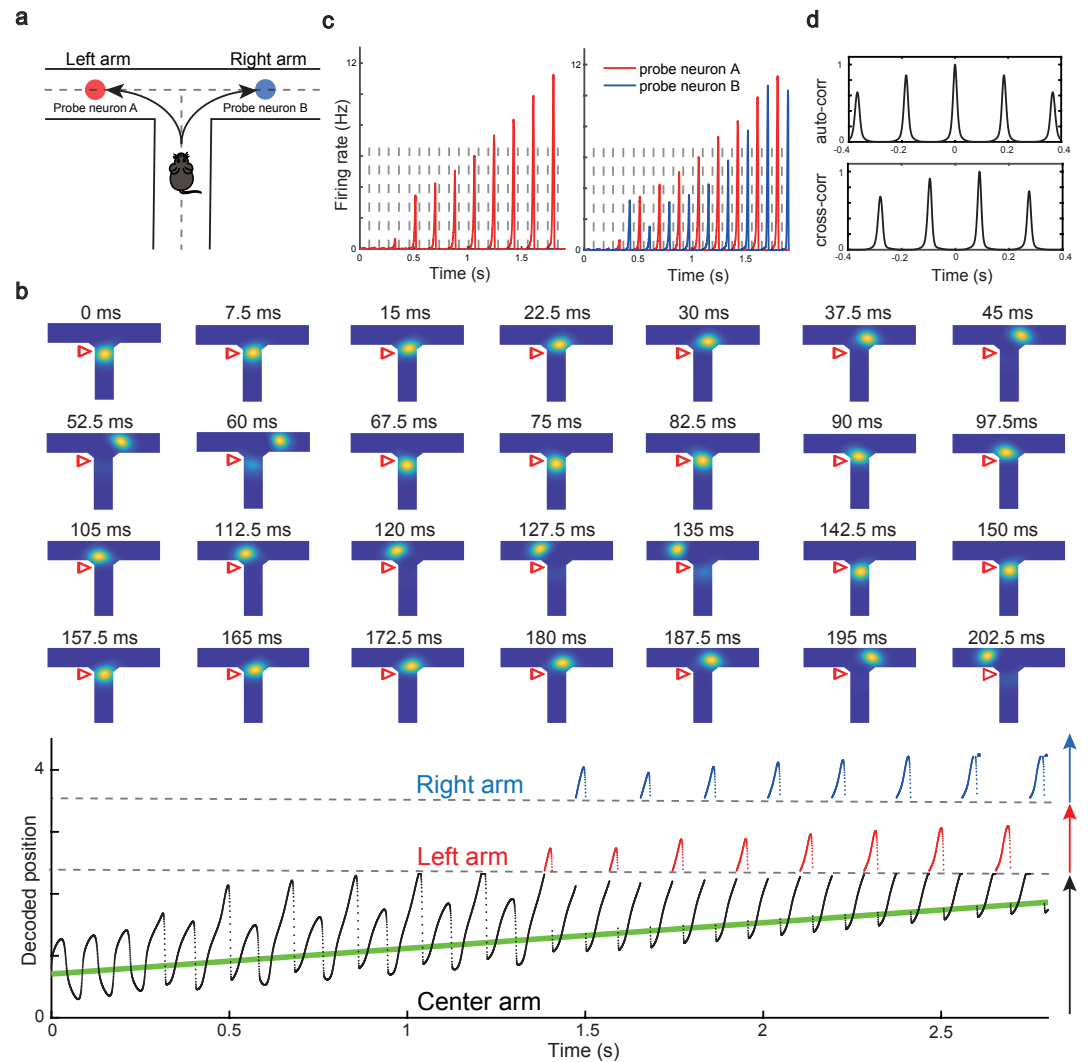


Figure 5. Constant cycling of future positions in a T-maze environment. **a**, An illustration of an animal navigating a T-maze environment with two possible upcoming choices (the left and right arms). **b**, Upper panel: Snapshots of constant cycling of theta sweeps on two arms when the animal is approaching the choice point. Red triangle marks the location of the external input. Note that the red triangle moves slightly towards the choice point in the 200 ms duration. Lower panel: Constant cycling of two possible future locations. The black, red and blue traces represent the bump location on the center, left and right arms, respectively. The green line marks the location of the external moving input. **c**, Left panel: the firing rate trace of a neuron A on the left arm when the animal approaches the choice point. Right panel: the firing rate traces of a pair of neurons when the animal approaches the choice point, with neuron A (red) on the left arm and neuron B (blue) on the right arm. Dashed lines separate theta cycles. **d**, Upper panel: the auto-correlogram of the firing rate trace of probe neuron A. Lower panel: the cross-correlogram between the firing rate trace of neuron A and the firing rate trace of neuron B.

316 more details).

317 Robust phase coding of position with place cells

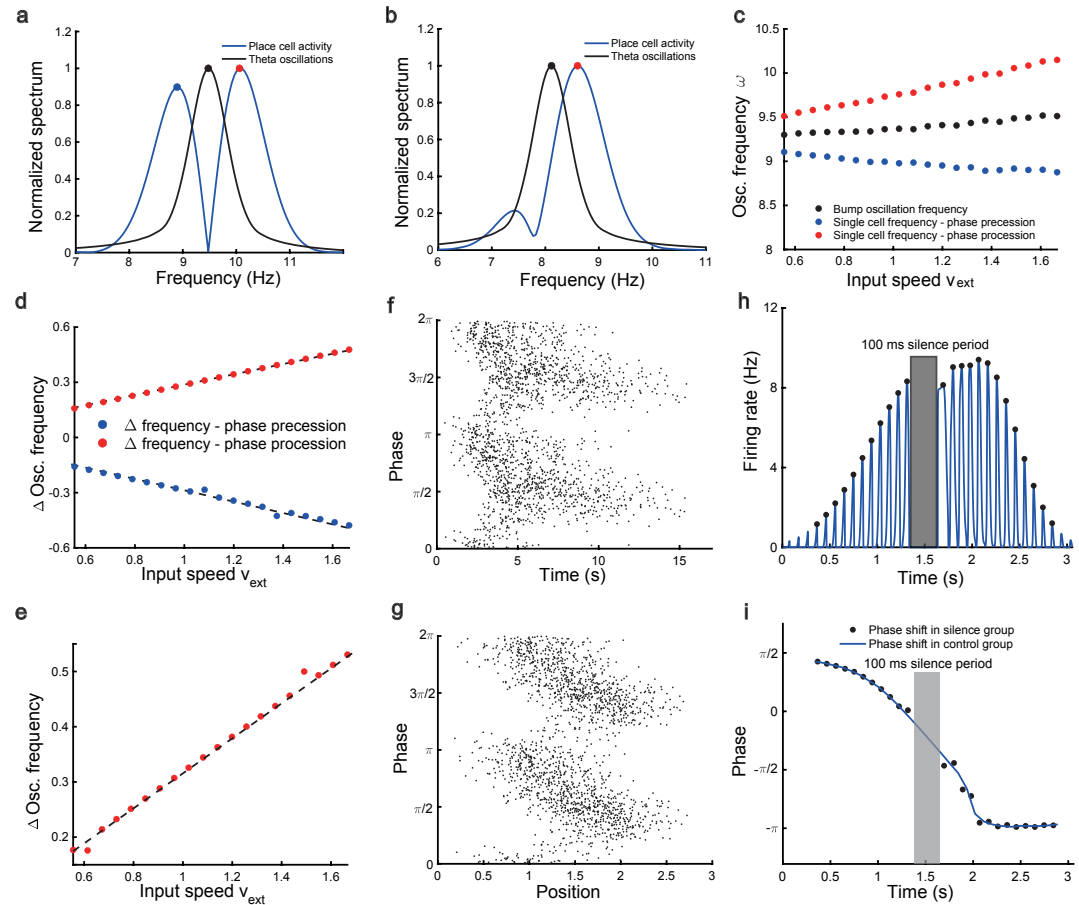


Figure 6. Robust phase coding of position. **a**, Normalized spectrum of bump oscillation (black curve) and the oscillation of a bimodal cell (blue curve). The black point marks the peak frequency of the bump oscillation (i.e. LFP theta). The blue and red points mark the peak frequencies of the oscillation of the bimodal cell. **b**, Normalized spectrum of bump oscillation and the oscillation of a unimodal cell. Note that the unimodal cell has only predominant phase precession and hence a single peak frequency (red point), which is higher than that of the bump oscillation. **c**, The peak frequency of bump oscillation versus moving speed (black points), and the oscillation of a bimodal cell versus moving speed (red and blue points). **d**, The difference in peak frequency between the oscillation of a bimodal cell and the bump oscillation versus moving speed. **e**, Same as **d** but for a unimodal cell. **f-g**, Theta phase as a function of time (**f**) or position (**g**). Each dot represents a spike generated through a Poisson process (see Method. for more details). **h**, Silencing the network activity for 100 ms (gray shaded area) when the external moving input passes through the center part of the place field of a unimodal cell. **i**, Theta phase shift of the unimodal cell with (black points) or without (blue curve) silencing the network.

318 As the firing rate shows large variability when the animal runs through the firing field (*Fenton*
 319 *and Muller, 1998*), it has been suggested that the theta phase shift provides an additional mech-
 320 anism to improve the localization of animals (*O'keefe and Burgess, 2005*). Indeed, (*Jensen and*
 321 *Lisman, 2000*) showed that taking phase into account leads to a significant improvement in the
 322 accuracy of localizing the animal. To demonstrate the robustness of phase coding, previous exper-
 323 iments showed two intriguing findings: a linear relationship between the firing frequency of place
 324 cells and the animal moving speed (*Geisler et al., 2007*), and the continued phase shift after inter-
 325 ruption of hippocampal activity (*Zugaro et al., 2005*). We show that our model can also reproduce
 326 these two phenomena.

327 To investigate the relationship between the single cell's oscillation frequency and the animal's

328 running speed, we consider a unimodal cell with predominant phase precession as studied in the
329 experiment (*Geisler et al., 2007*). Firstly, our model shows that the LFP theta frequency (the bump
330 oscillation frequency ω) is largely independent of the running speed of the animal (the speed of
331 the external input, see Eq. 6) (Fig. 6c). The phase precession implies that the oscillation frequency
332 of a place cell is higher than LFP theta frequency, since firing precesses to earlier phases over theta
333 cycles (Fig. 6a&b). Secondly, we can analytically quantify how the single cell's oscillation frequency is
334 modulated by the external moving speed. As shown in Sec. , the distance the animal travels during
335 the phase shift stage is $2c_0$, which gives the travelling time $T = 2c_0/v_{ext}$ and the number of theta
336 cycles for phase precession $K_f = T\omega$. Since the total amount of phase shift over the whole process
337 is π (i.e, half of the theta cycle, Fig. 3e), it means that K_f firing peaks are generated by a unimodal
338 cell within $T_f = (T\omega - 0.5)/\omega$ units of time. Thus, the firing frequency of the cell is calculated to be
339 $\omega_f = K_f/T_f \approx \omega + 0.25v_{ext}/c_0$ (where the condition $K_f \gg 0.5$ is used), which increases linearly with
340 the animal speed v_{ext} (Fig. 6c-e). This linear relationship ensures that the firing phase of a unimodal
341 cell in each theta cycle is locked with the relative location of the animal in the firing field of that cell,
342 which supports a robust phase-position code. Notably, in our model, the speed modulation of the
343 place cells' firing frequency is not the cause of theta phase shift, but rather a result of oscillatory
344 tracking. This is different from the dual oscillator model (*Lengyel et al., 2003*), which assumes that
345 phase precession is caused by a speed-dependent increase in the dendritic oscillation frequency
346 (see Discussion for more details).

347 In a different experiment, (*Zugaro et al., 2005*) found that the firing phase of a place cell contin-
348 ues to precess even after hippocampal activity was transiently silenced for up to 250 ms (around 2
349 theta cycles). To reproduce this phenomenon, we also study a unimodal cell by manually turning off
350 the network activity for a few hundred milliseconds (by setting $r(x, t) = 0$ for all neurons) and then
351 letting the network dynamics evolves again with all parameters unchanged. Based on the theoret-
352 ical analysis (Eq. 8), we see that the firing phase of a place cell is determined by the location of the
353 external input (i.e., $v_{ext}t$), which means that as the external input moves forward on the linear track,
354 the firing phase will precess accordingly in successive oscillatory cycles. Thus, once the network is
355 recovered to the oscillatory tracking state and the external input conveys the new location of the
356 animal to the network, phase precession is resumed from the new location. Therefore, the firing
357 phase in the first bump oscillation cycle after the network perturbation is more advanced than the
358 firing phase in the last bump oscillation cycle right before the perturbation, and the amount of
359 precession is similar to that in the case without perturbation (Fig. 6h&i). This agrees well with the
360 experimental observation, and indicates that the phase-position code is robust to the perturbation
361 of the hippocampal dynamics.

362 Overall, our model reproduces these two experimental findings, and suggests that there exists
363 a one-to-one correspondence between the firing phase of a place cell and the travelled distance in
364 the neuron's place field, which is independent of the animal's running speed or the perturbation
365 duration (Fig.S3). This agrees well with experimental observations (*O'Keefe and Recce, 1993*) that
366 theta phase correlates better with the animal's location than with time (Fig. 6f&g). In addition to
367 the results for unimodal cells as introduced above, our model predicts new results for bimodal
368 cells. First, in contrast to a unimodal cell, a bimodal cell will have two peaks in its firing frequency,
369 with one slightly higher than the LFP theta baseline (due to phase precession) and the other slightly
370 lower than the LFP theta baseline (due to phase precession). The precession-associated frequency
371 positively correlates with the running speed of the animal, while the procession-associated fre-
372 quency negatively correlates with the running speed (Fig. 6d). Second, similar to the preserved
373 phase shift in unimodal cells, both the phase precession and procession of a bimodal cell after
374 transient intrahippocampal perturbation continue from the new location of the animal (see SI), no
375 matter how long the silencing period lasts. The two predictions could be tested by experiments.

376 Discussion

377 Model contributions

378 In this paper, we have proposed a CANN with firing rate adaptation to unveil the underlying mech-
379 anism of place cell phase shift during locomotion. We show that the interplay between intrinsic
380 mobility (owing to firing rate adaptation) and extrinsic mobility (owing to the location-dependent
381 sensory inputs) leads to an oscillatory tracking state, which naturally accounts for theta sweeps
382 where the decoded position oscillates around the animal's physical location at the theta rhythm.
383 At the single neuron level, we show that the forward and backward bump sweeps account for,
384 respectively, phase precession and phase procession. Furthermore, we show that the varied adap-
385 tation strength explains the emergence of bimodal and unimodal cells, that is, as the adaptation
386 strength increases, forward sweeps of the bump gradually suppress backward sweeps, and as a
387 result, neurons initially exhibiting both significant phase precession and procession (due to a low
388 level adaptation) will gradually exhibit only predominant phase precession (due to a high level
389 adaptation).

390 Computational models for theta phase shift and theta sweeps

391 As a subject of network dynamics, oscillatory tracking has been studied previously in an excitatory-
392 inhibitory neural network (*Folias and Bressloff, 2004*), where it was found that decreasing the exter-
393 nal input strength can lead to periodic emission of traveling waves in the network (Hopf instability),
394 which is analogous to the oscillatory tracking state in our model. However, their focus was on the
395 mathematical analysis of such dynamical behavior, while our focus is on the biological implications
396 of oscillatory tracking, i.e., how can it be linked to phase precession and procession of hippocampal
397 place cells.

398 Due to their potential contributions to the temporal sequence learning involved in spatial navi-
399 gation and episodic memory (*Mehta et al., 1997, 2002; Yamaguchi, 2003*), theta phase precession
400 and forward theta sweeps have been modelled in the field for decades. These models can be di-
401 vided into two main categories, with one relying on the mechanism of single cell oscillation (*O'Keefe
402 and Recce, 1993; Kamondi et al., 1998; Lengyel et al., 2003; O'Keefe and Burgess, 2005; Mehta et al.,
403 2002*), and the other relying on the mechanism of recurrent interactions between neurons (*Tsodyks
404 et al., 1996; Romani and Tsodyks, 2015; Kang and DeWeese, 2019*). A representative example of
405 the former is the oscillatory interference model (*O'Keefe and Recce, 1993; Lengyel et al., 2003*),
406 which produces phase precession via the superposition of two oscillatory signals, with one from
407 the baseline somatic oscillation at the LFP theta frequency (reflecting the inputs from the medial
408 septal pacemaker (*Stewart and Fox, 1990*)), and the other from the dendritic oscillation whose
409 frequency is slightly higher. While these models can explain a large variety of experimental phe-
410 nomena, it remain unclear how oscillation of individual neurons has a frequency higher than the
411 baseline theta frequency. Here, our model provides a network mechanism for how such higher-
412 frequency oscillation emerges.

413 A representative model relying on neuronal recurrent interactions is the activation spreading
414 model (*Tsodyks et al., 1996*). This model produces phase precession via the propagation of neu-
415 ral activity along the movement direction, which relies on asymmetric synaptic connections. A
416 later version of this model considers short-term synaptic plasticity (short-term depression) to im-
417 plicitly implement asymmetric connections between place cells (*Romani and Tsodyks, 2015*), and
418 reproduces many other interesting phenomena, such as phase precession in different environ-
419 ments. However, since the asymmetric connections always skew towards the moving direction
420 (along which the connection strength is stronger than that in the opposite direction), the activity
421 bump can only propagate along the moving direction. Therefore, these two models only reproduce
422 theta phase precession. Rather than relying on neuronal asymmetric connections to induce activ-
423 ity spreading, our model considers firing rate adaptation at individual neurons, which allows the
424 activity bump to propagate in both directions alternately, and hence generate interleaved phase

425 precession and procession. Furthermore, to prevent the activity bump from spreading away, their
426 model considers an external theta input to reset the bump location at the end of each theta cycle,
427 whereas in our model, because of the oscillation of the bump, no external theta input is needed,
428 and by choosing the model parameters properly, the bump can oscillate at the theta rhythm. Never-
429 theless, experimental studies have suggested that hippocampal neurons receive theta modulation
430 from the medial septal pacemaker (*Stewart and Fox, 1990; King et al., 1998; Wang, 2002*). In our
431 model, if we include such an external theta input, the bump oscillation will be locked at the theta
432 rhythm more robustly without the need of fine tuning model parameters. Such a theta input may
433 also have the role of coordinating theta phase shifts across brain regions. We will investigate this
434 issue in future work.

435 **Beyond the linear track environment**

436 Besides the linear track environment, the mechanism of generating theta sweeps proposed in our
437 model can also be generalized to more complex environments. For instance, in a T-maze environ-
438 ment, our model explains the constant cycling of theta sweeps between left and right arms. Such
439 cycling behavior may be important for high-speed actions such as predating and escaping which
440 require animals to make decision among several future scenarios at the sub-second level. Similar
441 alternative activity sweeps in the T-maze environment has been studied in a previous paper (*Ro-*
442 *mani and Tsodyks, 2015*), which showed that the frequency of alternation correlates with overtly
443 deliberative behaviors such as head scans (frequency at 1 Hz or less) (*Johnson and Redish, 2007*).
444 In contrast to our model, the network activity in their model propagates continuously from the
445 current location on the center arm till the end of the outer arm, which takes a few theta cycles
446 (i.e., 1 second or more). In our model, the network bump alternately sweeps to one of the two
447 outer arms at a much higher frequency (~ 8 Hz), which may be related to fast decision-making
448 or planing in natural environments (*Kay et al., 2020*). Furthermore, our model can also be easily
449 extended to the multiple-arms (> 2) environment (*Gillespie et al., 2021*) or the cascade-T envi-
450 ronment (*Johnson and Redish, 2007*) with the underlying mechanism of generating theta cycling
451 remaining unchanged. In addition to the linear and T-maze environments, phase shift has also
452 been reported when an animal navigates in an open field environment. However, due to the lack
453 of recorded neurons, decoding theta sweeps in the 2D environment is not as straightforward as in
454 the 1D case. While theta sweeps in the 1D case have been associated with goal-directed behaviors
455 and spatial planning (*Wikenheiser and Redish, 2015*), it remains unclear whether such conclusion
456 is applicable to the 2D case. Our preliminary result shows that in the 2D CANN where neurons are
457 arranged homogeneously according to their relative firing locations, the activity bump will sweep
458 along the tangent direction of the movement trajectory, similar to the 1D case (see SI.4 and Fig.S4
459 for details). It will be interesting to explore theta sweeps in the open field environment in detail
460 when more experimental data is available.

461 **Model implications and future works**

462 In the current study, we have modeled the place cell population in the hippocampus with a CANN
463 and adopted firing rate adaptation to generate theta phase shift. In fact, this model can be easily
464 extended to the grid cell population without changing the underlying mechanism. For instance,
465 we can induce the torus-like connection profile (periodic boundary in the 2D space) (*Samsonovich*
466 *and McNaughton, 1997; McNaughton et al., 2006*) or the locally inhibitory connection profile (*Burak*
467 *and Fiete, 2009; Couey et al., 2013*) in the CANN structure to construct a grid cell model, and by
468 imposing firing rate adaptation, neurons in the grid cell network will also exhibit phase shift as
469 the animal moves through the grid field, as reported in previous experimental studies (*Hafting*
470 *et al., 2008; Van Der Meer and Redish, 2011*). Notably, although for both grid cells and place cells,
471 CANNs can generate theta phase shift, it does not mean that they are independent from each other.
472 Instead, they might be coordinated by the same external input from the environment, as well as by
473 the medial septum which is known to be a pacemaker that synchronises theta oscillations across

474 different brain regions (*King et al., 1998; Wang, 2002*). We will investigate this issue in future work.
475 Our model suggests that the “online” theta sweep and the “offline” replay may share some
476 common features in their underlying mechanisms (*Romani and Tsodyks, 2015; Hopfield, 2010;*
477 *Kang and DeWeese, 2019; Jahnke et al., 2015*). We have shown that the activity bump with strong
478 adaptation can move spontaneously when the external input becomes weak enough (see Sec.).
479 Such non-local spreading of neural activity has a speed much faster than the conventional speed
480 of animals (the external input speed in our model, see Fig. 2d), which resembles the fast spread-
481 ing of the decoded position during sharp-wave ripple events (*Diba and Buzsáki, 2007; Foster and*
482 *Wilson, 2006; Karlsson and Frank, 2009; Dragoi and Tonegawa, 2011*). This indicates that these
483 two phenomena may be generated by the same neural mechanism of firing rate adaptation, with
484 theta sweeps originating from the interplay between the adaptation and the external input, while
485 replay originating from only the adaptation, since the external input is relatively weak during the
486 “offline” state. This hypothesis seems to be supported by the coordinated emergence of theta se-
487 quences and replays during the post-natal development period (*Muessig et al., 2019*), as well as
488 their simultaneous degradation when the animal travelled passively on a model train (*Drieu et al.,*
489 *2018*).

490 Nevertheless, it is important to note that the CANN we adopt in the current study is an idealized
491 model for the place cell population, where many biological details are missed (*Amari, 1977; Tsodyks*
492 *and Sejnowski, 1995; Samsonovich and McNaughton, 1997; Tsodyks, 1999*). For instance, we have
493 assumed that neuronal synaptic connections are translation-invariant in the space. In practice,
494 such a connection pattern may be learned by a synaptic plasticity rule at the behavioral time scale
495 when the animal navigates actively in the environment (*Bittner et al., 2017*). In future work, we
496 will explore the detailed implementation of this connection pattern, as well as other biological
497 correspondences of our idealized model, to establish a comprehensive picture of how theta phase
498 shift is generated in the brain.

499 Materials and Methods

500 General summary of the model

501 We consider a one-dimensional continuous attractor neural network (1D CANN), in which neurons
502 are uniformly aligned according to their firing fields on a linear track (for the T-maze case, see
503 Methods. below; for the case of the open field (2D CANN), see SI.4). Denote $U(x, t)$ the synaptic
504 input received by the place cell at location x , and $r(x, t)$ the corresponding firing rate. The dynamics
505 of the network is written as

$$\tau \frac{dU(x, t)}{dt} = -U(x, t) + \rho \int_{-\infty}^{\infty} J(x, x') r(x', t) dx' - V(x, t) + I^{ext}(x, t), \quad (9)$$

506 where τ is the time constant of $U(x, t)$ and ρ the neuron density. The firing rate $r(x, t)$ is given by

$$r(x, t) = \frac{U(x, t)^2}{1 + k\rho \int_{-\infty}^{\infty} U(x', t) dx'}, \quad (10)$$

507 where k controls the strength of the global inhibition (divisive normalization). $J(x, x')$ denotes the
508 connection weight between place cells at location x and x' , which is written as:

$$J(x, x') = \frac{J_0}{2\pi a} \exp\left[-\frac{(x - x')^2}{2a^2}\right], \quad (11)$$

509 where J_0 controls the strength of the recurrent connection and a the range of neuronal interaction.
510 Notably, $J(x, x')$ depends on the relative distance between two neurons, rather than the absolute
511 locations of neurons. Such translation-invariant connection form is crucial for the neutral stability
512 of the attractor states of CANNs (*Wu et al., 2016*). $I^{ext}(x, t)$ represents the external input which
513 conveys the animal location information to the hippocampal network, which is written as:

$$I^{ext}(x, t) = \alpha \exp \left[-\frac{(x - v_{ext}t)^2}{4a^2} \right], \quad (12)$$

514 with v_{ext} denoting the animal's running speed and α controlling the input strength to the hippocam-
 515 pus. $V(x, t)$ denotes the adaptation effect of the place cell at location x , which increases with the
 516 synaptic input (and hence the place cell's firing rate), i.e.,

$$\tau_v \frac{dV(x, t)}{dt} = -V(x, t) + mU(x, t), \quad (13)$$

517 with τ_v denoting the time constant of $V(x, t)$ and m the adaptation strength. Note that $\tau_v \gg \tau$,
 518 meaning that adaptation is a much slower process compared to the neural firing.

519 Stability analysis of the bump state

520 We derive the condition under which the bump activity is the stable state of the CANN. For simplic-
 521 ity, we consider the simplest case that there is no external input and adaptation in the network, i.e.,
 522 $m = \alpha = 0$. In this case, the network state is determined by the strength of the recurrent excitation
 523 and global inhibition. When the global inhibition is strong (k is large), the network is silent, i.e., no
 524 bump activity emerges in the CANN. When the global inhibition is small, an activity bump with the
 525 Gaussian-shaped profile emerges, which is written as:

$$\bar{U}(x, t) = A_u \exp \left\{ -\frac{[x - z(t)]^2}{4a^2} \right\}, \quad (14)$$

$$\bar{r}(x, t) = A_r \exp \left\{ -\frac{[x - z(t)]^2}{2a^2} \right\}, \quad (15)$$

526 with A_u and A_r representing the amplitudes of the synaptic input bump and the firing rate bump,
 527 respectively. $z(t)$ represents the bump center, and a is the range of neuronal interaction (defined in
 528 Methods.). To solve the network dynamics, we substitute Eqs. 14&15 into Eqs. 9&10, which gives
 529 (see SI.2 for more details of the derivation):

$$\tau \frac{dA_u}{dt} = -A_u + \frac{\rho J_0}{\sqrt{2}} A_r, \quad (16)$$

$$A_r = \frac{A_u^2}{1 + \sqrt{2\pi k \rho a} A_u^2}, \quad (17)$$

530 These two equations describes how the bump amplitudes change with time. For instance, if neu-
 531 rons are weakly connected (small J_0) or they are connected sparsely (small ρ), the second term on
 532 the right-hand side of Eq. 16 is small, and A_u will decay to zero, implying that the CANN cannot
 533 sustain a bump activity. By setting $dA_u/dt = 0$, we obtain:

$$A_u = \frac{\rho J_0 \pm \sqrt{\rho^2 J_0^2 - 8\sqrt{2\pi} 2k\rho a}}{4\sqrt{\pi k \rho a}}, \quad (18)$$

$$A_r = \frac{\sqrt{2}}{\rho J_0} A_u. \quad (19)$$

534 It is straightforward to check that only when $k < k_c = \rho J_0^2 / 8\sqrt{2\pi} a$, A_u have two real solutions
 535 (indicated by the \pm sign in Eq. 18), i.e., the dynamic system (Eqs. 16&17) has two fixed points. It
 536 can be checked that only $A_u = \left(\rho J_0 + \sqrt{\rho^2 J_0^2 - 8\sqrt{2\pi} 2k\rho a} \right) / \left(4\sqrt{\pi k \rho a} \right)$ is the stable solution.

537 Analysis of intrinsic mobility of the bump state

538 We derive the condition under which the bump of the CANN moves spontaneously in the attractor
 539 space without relying on external inputs. As the adaptation strength increases, the bump activity

540 becomes unstable and has tendency to move away from its location spontaneously. Such intrinsic
 541 mobility of the CANN has been shown in previous studies (*Bressloff, 2011; Wu et al., 2016; Mi et al.,*
 542 *2014*). We set $\alpha = 0$ (no external input), and investigate the effect of adaptation strength m on the
 543 bump dynamics. Our simulation result shows that during the spontaneous movement, $V(x, t)$ can
 544 also be represented by a Gaussian-shaped bump, which is written as

$$\bar{V}(x, t) = A_v \exp \left\{ -\frac{[x - z(t) + d(t)]^2}{4a^2} \right\}, \quad (20)$$

545 where A_r denotes the amplitude of the adaptation bump, and $d(t)$ the displacement between the
 546 bump centers of $U(x, t)$ and $V(x, t)$. This displacement originates from the slow dynamics of adapta-
 547 tion, which leads to that the adaptation bump always lags behind the neural activity bump. Similar
 548 to Methods. , we substitute the bump profiles Eqs. (14, 15, 20) into the network dynamics Eqs. (9,
 549 10, 13), and obtain:

$$\begin{aligned} \tau \left[A_u \frac{x - z}{2a^2} \frac{dz}{dt} + \frac{dA_u}{dt} \right] \mathcal{N}(z, 2a) &= (-A_u + \frac{\rho J_0}{\sqrt{2}} A_r) \mathcal{N}(z, 2a) - A_v \mathcal{N}(z - d, 2a), \\ A_r &= \frac{A_u^2}{1 + k\rho\sqrt{2\pi}aA_u^2}, \\ \tau_v \left[A_v \frac{x - z + d}{2a^2} \frac{d(z - d)}{dt} + \frac{dA_v}{dt} \right] \mathcal{N}(z - d, 2a) &= -A_v \mathcal{N}(z - d, 2a) + mA_u \mathcal{N}(z, 2a), \end{aligned} \quad (21)$$

550 where $\mathcal{N}(z, 2a) = \exp \{ -[x - z]^2 / 4a^2 \}$.

551 Previous works have shown that the dynamics of a CANN is dominated by very few motion
 552 modes (*Fung et al., 2010, 2012*). To solve the CANN dynamics, we can project the network dynamics
 553 onto those dominating modes and simplify the analyses significantly. Here, we consider the first
 554 two motion modes, corresponding to the changes of the bump height and position, respectively,
 555 which are given by,

$$u_0(x, t) = \exp \left\{ -\frac{[x - z(t)]^2}{4a^2} \right\}, \quad (22)$$

$$u_1(x, t) = [x - z(t)] \exp \left\{ -\frac{[x - z(t)]^2}{4a^2} \right\}. \quad (23)$$

556 By projecting the network dynamics onto these two motion modes, we obtain:

$$(-A_u + \frac{\rho J_0}{\sqrt{2}} A_r) \sqrt{2\pi}a - A_v \exp(-\frac{d^2}{8a^2}) \sqrt{2\pi}a = 0, \quad (24)$$

$$-A_u + \frac{\rho J_0}{\sqrt{2}} A_r - A_v \exp(-\frac{d^2}{8a^2}) = 0, \quad (25)$$

$$\tau A_u v_{int} = d A_v \exp(-\frac{d^2}{8a^2}), \quad (26)$$

$$\frac{d}{4a^2} \tau_v A_v \exp(-\frac{d^2}{8a^2}) v_{int} = -A_v \exp(-\frac{d^2}{8a^2}) + mA_u, \quad (27)$$

$$\tau_v (1 - \frac{d^2}{4a^2}) v_{int} = d. \quad (28)$$

557 Eqs. 24-28 describes the relationships between bump features A_u , A_r , A_v , v_{int} and d . By solving these

558 equations, we obtain,

$$A_u = \frac{\rho J_0 + \sqrt{\rho^2 J_0^2 - 8\sqrt{2\pi k\rho a}(1 + \sqrt{\frac{m\tau}{\tau_v}})^2}}{4\sqrt{\pi k\rho a}(1 + \sqrt{\frac{m\tau}{\tau_v}})}, \quad (29)$$

$$A_v = \frac{\rho J_0 + \sqrt{\rho^2 J_0^2 - 8\sqrt{2\pi k\rho a}(1 + \sqrt{\frac{m\tau}{\tau_v}})^2}}{2\sqrt{2\pi k\rho^2 a}J_0}, \quad (30)$$

$$A_r = \sqrt{\frac{m\tau}{\tau_v}} \exp\left[\frac{1 - \sqrt{\frac{\tau}{m\tau_v}}}{2}\right] \frac{\rho J_0 + \sqrt{\rho^2 J_0^2 - 8\sqrt{2\pi k\rho a}(1 + \sqrt{\frac{m\tau}{\tau_v}})^2}}{4\sqrt{\pi k\rho a}(1 + \sqrt{\frac{m\tau}{\tau_v}})}, \quad (31)$$

$$d = 2a\sqrt{1 - \sqrt{\frac{\tau}{m\tau_v}}}, \quad (32)$$

$$v_{int} = \frac{2a}{\tau_v} \sqrt{\frac{m\tau_v}{\tau} - \sqrt{\frac{m\tau_v}{\tau}}}. \quad (33)$$

559 Eqs. 29-31 describe the amplitudes of the bumps of synaptic input, firing rate, and adaptation in
 560 the CANN, respectively, and Eq. 32 describes the displacement between the neural activity and
 561 adaptation bumps. From Eq. 33, we see that for the bump to travel spontaneously, it requires
 562 $m > \tau/\tau_v$, i.e., the adaptation strength is larger than a threshold given by the ratio between two
 563 time constants τ and τ_v . As the adaptation strength increases (larger m), the travelling speed of the
 564 bump increases (larger v_{int}).

565 Analysis of the oscillatory tracking behaviour of the bump state

566 When both the external input and the adaptation are applied to the CANN, the bump activity can
 567 oscillate around the external input if the strengths of the external input and the adaptation are
 568 appropriated. The simulation shows that during the oscillatory tracking, the bump shape is roughly
 569 unchanged, and the oscillation of the bump center can be approximated as a sinusoidal wave
 570 expressed as:

$$z(t) = c_0 \sin(\omega t) + d_0 + v_{ext}t, \quad (34)$$

571 where c_0 and ω denote, respectively, the oscillation amplitude and frequency, and d_0 denotes a
 572 constant offset between the oscillation center and the external input.

573 Similar to the analysis in Methods. , we substitute the expression of $z(t)$ (Eq. 34) into Eqs. (14,
 574 15, 20), and then simplify the network dynamics by applying the projection method (see SI.3 for
 575 more detailed derivation). We obtain,

$$(m+1)A_u - \frac{\rho J_0}{\sqrt{2}} \frac{A_u^2}{1 + \sqrt{2\pi a k \rho} A_u^2} - \alpha = 0, \quad (35)$$

$$\omega^2 = \frac{\alpha}{\tau \tau_v A_u}, \quad (36)$$

$$mA_u \exp\left(-\frac{d^2}{8a^2}\right) = A_v, \quad (37)$$

$$d_0 = \tau_v v, \quad (38)$$

$$\sqrt{\frac{2(\tau A_u + \alpha \tau_v)}{\alpha \tau_v}} \left[4a^2 \left(\ln \frac{\tau_v mA_u}{\tau A_u + \alpha \tau_v} \right) - \tau_v^2 v^2 \right] = c_0, \quad (39)$$

576 Eqs. 35-39 describe the relationships among 6 oscillation features A_u, A_r, A_v, c_0, d_0 and ω . By solving

577 these equations, we obtain:

$$A_u = \frac{J_0 + 2\sqrt{\pi}ak\alpha}{2\sqrt{\pi}ak(1+m)}, \quad (40)$$

$$A_r = \frac{A_u^2}{1 + \sqrt{2\pi}ak\rho A_u^2}, \quad (41)$$

$$A_v = \sqrt{\left(\frac{\tau A_u + \alpha\tau_v}{\tau_v}\right) mA_u}, \quad (42)$$

$$c_0 = A_v \sqrt{\frac{2}{\alpha mA_u} \left[8a^2 \ln \frac{mA_u}{A_v} - \tau_v^2 v^2 \right]}, \quad (43)$$

$$d_0 = \tau_v v, \quad (44)$$

$$\omega = \sqrt{\frac{\alpha}{\tau\tau_v A_u}}. \quad (45)$$

578 It can be seen from Eq. 43 that for the bump activity to oscillate around the external input (i.e.,
 579 the oscillation amplitude $c_0 > 0$), it requires that $8a^2 \ln(mA_u/A_v) - \tau_v^2 v^2 > 0$. This condition gives the
 580 boundary (on the parameter values of the input strength α and the adaptation strength m) that
 581 separate two tracking states, i.e., smooth tracking and oscillatory tracking (see Fig. 2g and Fig.S1
 582 for the comparison between the simulation results and theoretical results).

583 Note that to get the results in Eqs. 35-39, we have assumed that the amplitudes of neural activity
 584 bumps and the adaptation bump remain unchanged during the oscillation (i.e., A_u, A_v, A_r are con-
 585 stants). However, this assumption is not satisfied when the SFA strength m is large (see Sec. and
 586 Fig. 4). In such a case, we carry out simulation to analyze the network dynamics.

587 **Implementation details of the linear track environment**

588 For the linear track environment, we simulate an 1D CANN with 512 place cells topographically
 589 organized on the one-dimensional neuronal track. Since we are interested in how the neuronal
 590 firing phase shifts as the animal moves through the firing field of a place cell, we investigate the
 591 place cell at location $x = 0$ and ignore the boundary effect, that is, we treat the linear track with the
 592 infinite length. The neural firing time constant is set to be 3 ms, while the time constant of spike
 593 frequency adaptation is much longer, which is set to be 144 ms. The density of place cells on the
 594 linear track is set to be $256/\pi$. The excitatory interaction range of place cells is set to be $0.4m$, while
 595 the maximum excitatory connection strength J_0 is set to be 0.2. The gain factor is set to be 5. The
 596 global inhibition strength k is set to be 5. The moving speed of the virtual animal v_{ext} is set to be 1.5
 597 m/s. For the simulation details, we use the first-order Euler method with the time step δt set to be
 598 0.3 the duration of simulation T set to be 10 s. These parameters are commonly used in all plots
 599 related to the linear track environment (see Table.1 for a summary).

600 For the two key parameters, i.e., the external input strength α and the adaptation strength m , we
 601 vary their values in different plots. Specifically, for illustrating the smooth tracking state in Fig. 2c,
 602 we set $\alpha = 0.19$ and $m = 0$. For illustrating the travelling wave state (intrinsic mobility of the bump
 603 state) in Fig. 2d, we set $\alpha = 0$ and $m = 0.31$. For plotting the relationship between the intrinsic speed
 604 v_{int} and the adaptation strength m shown in Fig. 2e, we keep $\alpha = 0$, but vary m in the range between
 605 0 and 0.1 with a step of 0.05. For plotting the overall phase diagram including all three moving states
 606 as shown in Fig. 2g, we vary α in the range between 0.05 and 0.16 with a step of 0.001, and m in the
 607 range between 0.9 and 1.8 with a step of 0.01. To generate bimodal cell firing patterns in Fig. 3a and
 608 Fig. 4a,e&g, we choose $\alpha = 0.19$ and $m = 3.02$. To generate unimodal firing patterns in Fig. 4b,f&h,
 609 we choose $\alpha = 0.19$ but a relatively larger adaptation strength with $m = 3.125$. The values of these
 610 two parameters in different plots are summarized in Table. 2.

Table 1. Commonly used parameter values in the simulation of the linear track environment.

Parameters	Values
Number of place cells: N	512
Time constant of neural firing: τ	3ms
Time constant of spike frequency adaptation: τ_v	144ms
Neuron density: ρ	$256/\pi$
Recurrent connection range (Gaussian width): a	0.4 m
Recurrent connection strength: J_0	0.2
Gain factor: g	5
Global inhibition strength: k	5
Moving speed of the external input: v_{ext} (m/s)	1.5
Time interval: δt	0.3 s
Simulation duration: T	10 s

Table 2. Figure specific parameter values for input strength α and adaptation strength m .

Figures/parameters	α	m
An example of smooth tracking (Fig. 2c)	0.19	0
An example of traveling wave (Fig. 2d)	0	0.31
Intrinsic speed vs. adaptation strength (Fig. 2e)	0	0:0.05:0.1
Phase diagram (Fig. 2g)	0.05:0.001:0.16	0.9:0.01:1.8
Oscillatory tracking (bimodal) (Fig. 4a,e,g)	0.19	3.02
Oscillatory tracking (unimodal) (Fig. 4b,f,h)	0.19	3.125

611 Implementation details of the T-maze environment

612 Parameter configurations during simulation

613 To simulate the T-maze environment, we consider a CANN in which place cells are topographically
 614 organized in a T-shaped area which consists of a vertical central arm and two horizontal left and
 615 right arms (Fig. 5a). The width of the central arm is set to be 0.84 m and the length is set to be 3.14
 616 m. The widths of the two horizontal arms are also set to be 0.84 m, while the lengths of both arms
 617 are set to be 2.36 m. The connection strength between two neurons is determined by the distance
 618 between them, which is written as:

$$J(x, x'; y, y') = \frac{J_0}{2\pi a^2} \exp\left[-\frac{(x-x')^2 + (y-y')^2}{2a^2}\right]. \quad (46)$$

619 Here (x, y) and (x', y') represent the coordinates of two neurons in the T-maze environment, a is the
 620 recurrent connection range which is set to be 0.3, and J_0 controls the connection strength which is
 621 set to be 0.0125. Since we are interested in investigating theta sweeps when the animal is running
 622 on the central arm towards the junction point, the external input is restricted on the central arm
 623 which is modelled by a Gaussian-like moving bump written as:

$$I^{ext}(x, y) = \alpha \exp\left[-\frac{(x-x_0)^2 + (y-y_0)^2}{2a^2}\right], \quad (47)$$

624 where $x_0 = 0$ and $y_0 = v_{ext}t$ represent the center location of the external input with a moving speed
 625 $v_{ext} = 1.5$ m/s. In the simulation, we used the first-order Euler method with the time step $\delta t = 0.3$ s
 626 and the duration of simulation $T = 4.2$ s. The parameters used are summarized in Table.3.

627 Calculating auto-correlogram and cross-correlogram

628 To show the “cycle skipping” effect of a single place cell in the T-maze environment, we calculate
 629 the auto-correlogram of the firing rate trace of a place cell whose firing field encodes a location on
 630 the left arm (the upper panel in Fig. 5d). Assume the firing trace of the place cell is $f(t)$ (showed in
 631 left panel in Fig. 5c), the auto-correlogram is calculated as:

Table 3. Parameters values in the simulation of the T-maze environment

Parameters	Values
Number of cells central/left/right: N_1, N_2, N_3	3000/1500/1500
Time constant of neural firing: τ	3 ms
Time constant of spike frequency adaptation: τ_v	144 ms
Neuron density: ρ	$(128/\pi)^2$
Recurrent connection range (Gaussian width): a	0.3
Recurrent connection strength: J_0	$1.25 * 10^{-2}$
Gain factor: g	20
Global inhibition strength: k	1.25
Moving speed of the external input: v_{ext} (m/s)	1.5
Input strength: α	2
Adaptation strength: m	3.96
Time interval: δt	0.3 s
Simulation duration: T	3.3 s

$$(f * f)(\tau) \triangleq \int_{-\infty}^{\infty} f(t)f(t + \tau)dt, \quad (48)$$

632 where τ represents the time offset.

633 To show the “alternative cycling” effect of a pair of place cells with each of them encoding a
 634 location on each of the two outward arms, we calculate the cross-correlogram between their firing
 635 traces (the lower panel in Fig. 5d). It measures the similarity of the two firing traces as a function
 636 of the temporal offset of one relative to the other. Assume the firing traces of the two place cells
 637 are $f(t)$ and $g(t)$, respectively, the cross-correlogram is calculated as:

$$(f * g)(\tau) \triangleq \int_{-\infty}^{\infty} f(t)g(t + \tau)dt, \quad (49)$$

638 where τ represents the time offset.

639 **Details of generating the probability heatmap of theta phase shift**

640 In Fig. 4g&h we described the smoothed probability heatmaps of theta phase versus normalized
 641 position in the place field of both bimodal and unimodal cells. Generally, these two plots are simi-
 642 lar to the traditional spike plot of phase and position traveled in the place field (*O’Keefe and Recce,*
 643 *1993; Skaggs et al., 1996*). However, in our rate-based model, the phase of neuronal spike is not di-
 644 rectly modelled, rather we use the phase of firing rate peak to represent the phase shift in neuronal
 645 firing. Here we describe the implementation details of generating the heatmaps.

646 The x-axis denotes the normalized position in the place field, with -1 representing the position
 647 where the animal just enters the place field, and 1 representing the position where the animal just
 648 leaves the place field. In our simulation, the firing field of a place cell with preferred location at
 649 x_0 is defined as $x \in (x_0 - 2.5 * a, x_0 + 2.5a)$, with a roughly the half size of the firing field. Consider
 650 the animal is at x_t at time t (note that $x_t = v_{ext}t$), then its normalized position \tilde{x}_t is calculated as
 651 $\tilde{x}_t = (x_t - x_0)/(5a)$. The y-axis represents the phase of neuronal activity, which is in the range of
 652 $(0^\circ, 720^\circ)$. To calculate the phase at every time step, we divide the duration of the animal traversing
 653 the linear track into multiple theta cycles according to the bump’s oscillation. We can calculate the
 654 phase by $\theta_t = (t - t_0)/T$, with t_0 referring to the beginning of the present theta cycle and T referring
 655 to the theta period. Denote the firing rate of the i -th neuron at time t as $r_i(\tilde{x}_t, \theta_t)$, the probability
 656 heatmap is calculated by,

$$p(\tilde{x}, \theta_t) = C \sum_{i=1}^{N_c} \theta_i r_i(\tilde{x}, \theta_t), \quad (50)$$

657 where $C = 1 / \sum_t \sum_{i=1}^{N_c} \theta_i r_i(\tilde{x}, \theta_t)$ is the normalization factor.

658 **Spike generation from the firing rate**

659 To understand phase shift based on spiking time rather than the peak firing rate, we convert the
660 firing rate into spike trains according to the Poisson statistics (note that our analysis is rate-based,
661 but converting to spike-based does not change the underlying mechanism). For the i th place cell
662 which encodes position x_i on the linear track, the number of spikes n_i it generates within a time
663 interval Δt satisfies a Poisson distribution, which is expressed as,

$$P(n_i|z) = \frac{[f_i(z)\Delta t]^{n_i}}{n_i!} e^{-f_i(z)\Delta t}, \quad (51)$$

664 where z is the animal's location, and $f_i(z)$ is the tuning function of cell i , which is given by

$$f_i(z) = A_r \exp\left[-\frac{(x_i - z)^2}{2a^2}\right], \quad (52)$$

665 where A_r denotes the amplitude of the neural activity bump and a the range of recurrent interac-
666 tion.

References

- 667
668 Alonso, A. and Klink, R. (1993). Differential electroresponsiveness of stellate and pyramidal-like cells of medial
669 entorhinal cortex layer ii. *Journal of neurophysiology*, 70(1):128–143.
- 670 Amari, S.-i. (1977). Dynamics of pattern formation in lateral-inhibition type neural fields. *Biological cybernetics*,
671 27(2):77–87.
- 672 Azizi, A. H., Wiskott, L., and Cheng, S. (2013). A computational model for preplay in the hippocampus. *Frontiers*
673 *in computational neuroscience*, 7:161.
- 674 Battaglia, F. P. and Treves, A. (1998). Attractor neural networks storing multiple space representations: a model
675 for hippocampal place fields. *Physical Review E*, 58(6):7738.
- 676 Benda, J. and Herz, A. V. (2003). A universal model for spike-frequency adaptation. *Neural computation*,
677 15(11):2523–2564.
- 678 Bittner, K. C., Milstein, A. D., Grienberger, C., Romani, S., and Magee, J. C. (2017). Behavioral time scale synaptic
679 plasticity underlies ca1 place fields. *Science*, 357(6355):1033–1036.
- 680 Brandon, M. P., Bogaard, A. R., Schultheiss, N. W., and Hasselmo, M. E. (2013). Segregation of cortical head
681 direction cell assemblies on alternating theta cycles. *Nature neuroscience*, 16(6):739–748.
- 682 Bressloff, P. C. (2011). Spatiotemporal dynamics of continuum neural fields. *Journal of Physics A: Mathematical*
683 *and Theoretical*, 45(3):033001.
- 684 Burak, Y. and Fiete, I. R. (2009). Accurate path integration in continuous attractor network models of grid cells.
685 *PLoS computational biology*, 5(2):e1000291.
- 686 Burgess, N., Recce, M., and O’Keefe, J. (1994). A model of hippocampal function. *Neural networks*, 7(6-7):1065–
687 1081.
- 688 Couey, J. J., Witoelar, A., Zhang, S.-J., Zheng, K., Ye, J., Dunn, B., Czajkowski, R., Moser, M.-B., Moser, E. I., Roudi, Y.,
689 et al. (2013). Recurrent inhibitory circuitry as a mechanism for grid formation. *Nature neuroscience*, 16(3):318–
690 324.
- 691 Deshmukh, S. S., Yoganarasimha, D., Voicu, H., and Knierim, J. J. (2010). Theta modulation in the medial and
692 the lateral entorhinal cortices. *Journal of neurophysiology*, 104(2):994–1006.
- 693 Diba, K. and Buzsáki, G. (2007). Forward and reverse hippocampal place-cell sequences during ripples. *Nature*
694 *neuroscience*, 10(10):1241–1242.
- 695 Dong, X., Chu, T., Huang, T., Ji, Z., and Wu, S. (2021). Noisy adaptation generates lévy flights in attractor neural
696 networks. *Advances in Neural Information Processing Systems*, 34:16791–16804.
- 697 Dragoi, G. and Tonegawa, S. (2011). Preplay of future place cell sequences by hippocampal cellular assemblies.
698 *Nature*, 469(7330):397–401.
- 699 Drieu, C., Todorova, R., and Zugaro, M. (2018). Nested sequences of hippocampal assemblies during behavior
700 support subsequent sleep replay. *Science*, 362(6415):675–679.
- 701 Feng, T., Silva, D., and Foster, D. J. (2015). Dissociation between the experience-dependent development of
702 hippocampal theta sequences and single-trial phase precession. *Journal of Neuroscience*, 35(12):4890–4902.
- 703 Fenton, A. A. and Muller, R. U. (1998). Place cell discharge is extremely variable during individual passes of the
704 rat through the firing field. *Proceedings of the National Academy of Sciences*, 95(6):3182–3187.
- 705 Fernández-Ruiz, A., Oliva, A., Nagy, G. A., Maurer, A. P., Berényi, A., and Buzsáki, G. (2017). Entorhinal-ca3
706 dual-input control of spike timing in the hippocampus by theta-gamma coupling. *Neuron*, 93(5):1213–1226.
- 707 Foliás, S. E. and Bressloff, P. C. (2004). Breathing pulses in an excitatory neural network. *SIAM Journal on Applied*
708 *Dynamical Systems*, 3(3):378–407.
- 709 Foster, D. J., Morris, R. G., and Dayan, P. (2000). A model of hippocampally dependent navigation, using the
710 temporal difference learning rule. *Hippocampus*, 10(1):1–16.
- 711 Foster, D. J. and Wilson, M. A. (2006). Reverse replay of behavioural sequences in hippocampal place cells during
712 the awake state. *Nature*, 440(7084):680–683.

- 713 Foster, D. J. and Wilson, M. A. (2007). Hippocampal theta sequences. *Hippocampus*, 17(11):1093–1099.
- 714 Fuhrmann, G., Markram, H., and Tsodyks, M. (2002). Spike frequency adaptation and neocortical rhythms.
715 *Journal of neurophysiology*, 88(2):761–770.
- 716 Fung, C., Wong, K., and Wu, S. (2012). Delay compensation with dynamical synapses. *Advances in Neural Infor-*
717 *mation Processing Systems*, 25.
- 718 Fung, C. A., Wong, K. M., and Wu, S. (2010). A moving bump in a continuous manifold: a comprehensive study
719 of the tracking dynamics of continuous attractor neural networks. *Neural Computation*, 22(3):752–792.
- 720 Geisler, C., Robbe, D., Zugaro, M., Sirota, A., and Buzsáki, G. (2007). Hippocampal place cell assemblies are
721 speed-controlled oscillators. *Proceedings of the National Academy of Sciences*, 104(19):8149–8154.
- 722 Gillespie, A. K., Maya, D. A. A., Denovellis, E. L., Liu, D. F., Kastner, D. B., Coulter, M. E., Roumis, D. K., Eden,
723 U. T., and Frank, L. M. (2021). Hippocampal replay reflects specific past experiences rather than a plan for
724 subsequent choice. *Neuron*, 109(19):3149–3163.
- 725 Hafting, T., Fyhn, M., Bonnevie, T., Moser, M.-B., and Moser, E. I. (2008). Hippocampus-independent phase
726 precession in entorhinal grid cells. *Nature*, 453(7199):1248–1252.
- 727 Hao, J., Wang, X.-d., Dan, Y., Poo, M.-m., and Zhang, X.-h. (2009). An arithmetic rule for spatial summation
728 of excitatory and inhibitory inputs in pyramidal neurons. *Proceedings of the National Academy of Sciences*,
729 106(51):21906–21911.
- 730 Harris, K. D., Henze, D. A., Hirase, H., Leinekugel, X., Dragoi, G., Czurkó, A., and Buzsáki, G. (2002). Spike train
731 dynamics predicts theta-related phase precession in hippocampal pyramidal cells. *Nature*, 417(6890):738–
732 741.
- 733 Hassabis, D., Kumaran, D., Vann, S. D., and Maguire, E. A. (2007). Patients with hippocampal amnesia cannot
734 imagine new experiences. *Proceedings of the National Academy of Sciences*, 104(5):1726–1731.
- 735 Hopfield, J. J. (2010). Neurodynamics of mental exploration. *Proceedings of the National Academy of Sciences*,
736 107(4):1648–1653.
- 737 Jahnke, S., Timme, M., and Memmesheimer, R.-M. (2015). A unified dynamic model for learning, replay, and
738 sharp-wave/ripples. *Journal of Neuroscience*, 35(49):16236–16258.
- 739 Jaramillo, J. and Kempter, R. (2017). Phase precession: a neural code underlying episodic memory? *Current*
740 *opinion in neurobiology*, 43:130–138.
- 741 Jensen, O. and Lisman, J. E. (2000). Position reconstruction from an ensemble of hippocampal place cells:
742 contribution of theta phase coding. *Journal of neurophysiology*, 83(5):2602–2609.
- 743 Johnson, A. and Redish, A. D. (2007). Neural ensembles in ca3 transiently encode paths forward of the animal
744 at a decision point. *Journal of Neuroscience*, 27(45):12176–12189.
- 745 Kamondi, A., Acsády, L., Wang, X.-J., and Buzsáki, G. (1998). Theta oscillations in somata and dendrites of
746 hippocampal pyramidal cells in vivo: Activity-dependent phase-precession of action potentials. *Hippocampus*,
747 8(3):244–261.
- 748 Kang, L. and DeWeese, M. R. (2019). Replay as wavefronts and theta sequences as bump oscillations in a grid
749 cell attractor network. *Elife*, 8:e46351.
- 750 Karlsson, M. P. and Frank, L. M. (2009). Awake replay of remote experiences in the hippocampus. *Nature*
751 *neuroscience*, 12(7):913–918.
- 752 Kay, K., Chung, J. E., Sosa, M., Schor, J. S., Karlsson, M. P., Larkin, M. C., Liu, D. F., and Frank, L. M. (2020). Constant
753 sub-second cycling between representations of possible futures in the hippocampus. *Cell*, 180(3):552–567.
- 754 King, C., Recce, M., and O'keefe, J. (1998). The rhythmicity of cells of the medial septum/diagonal band of broca
755 in the awake freely moving rat: relationships with behaviour and hippocampal theta. *European Journal of*
756 *Neuroscience*, 10(2):464–477.
- 757 Lengyel, M., Szatmáry, Z., and Érdi, P. (2003). Dynamically detuned oscillations account for the coupled rate
758 and temporal code of place cell firing. *Hippocampus*, 13(6):700–714.

- 759 Losonczy, A., Zemelman, B. V., Vaziri, A., and Magee, J. C. (2010). Network mechanisms of theta related neuronal
760 activity in hippocampal ca1 pyramidal neurons. *Nature neuroscience*, 13(8):967–972.
- 761 McNaughton, B. L., Battaglia, F. P., Jensen, O., Moser, E. I., and Moser, M.-B. (2006). Path integration and the
762 neural basis of the ‘cognitive map’. *Nature Reviews Neuroscience*, 7(8):663–678.
- 763 Mehta, M., Lee, A., and Wilson, M. (2002). Role of experience and oscillations in transforming a rate code into
764 a temporal code. *Nature*, 417(6890):741–746.
- 765 Mehta, M. R., Barnes, C. A., and McNaughton, B. L. (1997). Experience-dependent, asymmetric expansion of
766 hippocampal place fields. *Proceedings of the National Academy of Sciences*, 94(16):8918–8921.
- 767 Mi, Y., Fung, C., Wong, K., and Wu, S. (2014). Spike frequency adaptation implements anticipative tracking in
768 continuous attractor neural networks. *Advances in neural information processing systems*, 27.
- 769 Muessig, L., Lasek, M., Varsavsky, I., Cacucci, F., and Wills, T. J. (2019). Coordinated emergence of hippocampal
770 replay and theta sequences during post-natal development. *Current Biology*, 29(5):834–840.
- 771 O’keefe, J. and Burgess, N. (2005). Dual phase and rate coding in hippocampal place cells: theoretical signifi-
772 cance and relationship to entorhinal grid cells. *Hippocampus*, 15(7):853–866.
- 773 O’Keefe, J. and Recce, M. L. (1993). Phase relationship between hippocampal place units and the eeg theta
774 rhythm. *Hippocampus*, 3(3):317–330.
- 775 Pfeiffer, B. E. (2020). The content of hippocampal “replay”. *Hippocampus*, 30(1):6–18.
- 776 Romani, S. and Tsodyks, M. (2015). Short-term plasticity based network model of place cells dynamics. *Hip-
777 pocampus*, 25(1):94–105.
- 778 Samsonovich, A. and McNaughton, B. L. (1997). Path integration and cognitive mapping in a continuous attrac-
779 tor neural network model. *Journal of Neuroscience*, 17(15):5900–5920.
- 780 Schmidt, R., Diba, K., Leibold, C., Schmitz, D., Buzsáki, G., and Kempter, R. (2009). Single-trial phase precession
781 in the hippocampus. *Journal of Neuroscience*, 29(42):13232–13241.
- 782 Skaggs, W. E., McNaughton, B. L., Wilson, M. A., and Barnes, C. A. (1996). Theta phase precession in hippocampal
783 neuronal populations and the compression of temporal sequences. *Hippocampus*, 6(2):149–172.
- 784 Stewart, M. and Fox, S. E. (1990). Do septal neurons pace the hippocampal theta rhythm? *Trends in neuro-
785 sciences*, 13(5):163–169.
- 786 Tsodyks, M. (1999). Attractor neural network models of spatial maps in hippocampus. *Hippocampus*, 9(4):481–
787 489.
- 788 Tsodyks, M. and Sejnowski, T. (1995). Associative memory and hippocampal place cells. *International journal of
789 neural systems*, 6:81–86.
- 790 Tsodyks, M. V., Skaggs, W. E., Sejnowski, T. J., and McNaughton, B. L. (1996). Population dynamics and theta
791 rhythm phase precession of hippocampal place cell firing: a spiking neuron model. *Hippocampus*, 6(3):271–
792 280.
- 793 Van Der Meer, M. A. and Redish, A. D. (2011). Theta phase precession in rat ventral striatum links place and
794 reward information. *Journal of neuroscience*, 31(8):2843–2854.
- 795 Van Strien, N., Cappaert, N., and Witter, M. (2009). The anatomy of memory: an interactive overview of the
796 parahippocampal–hippocampal network. *Nature reviews neuroscience*, 10(4):272–282.
- 797 Wang, M., Foster, D. J., and Pfeiffer, B. E. (2020). Alternating sequences of future and past behavior encoded
798 within hippocampal theta oscillations. *Science*, 370(6513):247–250.
- 799 Wang, X.-J. (2002). Pacemaker neurons for the theta rhythm and their synchronization in the septohippocampal
800 reciprocal loop. *Journal of neurophysiology*, 87(2):889–900.
- 801 Wikenheiser, A. M. and Redish, A. D. (2015). Hippocampal theta sequences reflect current goals. *Nature neuro-
802 science*, 18(2):289–294.
- 803 Wu, S., Hamaguchi, K., and Amari, S.-i. (2008). Dynamics and computation of continuous attractors. *Neural
804 computation*, 20(4):994–1025.

- 805 Wu, S., Wong, K. M., Fung, C. A., Mi, Y., and Zhang, W. (2016). Continuous attractor neural networks: candidate
806 of a canonical model for neural information representation. *F1000Research*, 5.
- 807 Yamaguchi, Y. (2003). A theory of hippocampal memory based on theta phase precession. *Biological cybernetics*,
808 89(1):1–9.
- 809 Yamaguchi, Y., Aota, Y., McNaughton, B. L., and Lipa, P. (2002). Bimodality of theta phase precession in hip-
810 pocampal place cells in freely running rats. *Journal of neurophysiology*, 87(6):2629–2642.
- 811 Zugaro, M. B., Monconduit, L., and Buzsáki, G. (2005). Spike phase precession persists after transient intrahip-
812 pocampal perturbation. *Nature neuroscience*, 8(1):67–71.

813 **Acknowledgements**

814 We thank Brad Pheiffer for sharing the data. We also thank Brad Pheiffer, Cheng Wang, Li Yao for
815 valuable discussions.

816 **Funding:** This work was support by: Science and Technology Innovation 2030-Brain Science and
817 Brain-inspired Intelligence Project (No. 2021ZD0200204, SW; No. 2021ZD0203700 / 2021ZD0203705,
818 YM), the Wellcome Principal Research Fellowship (NB), the National Natural Science Foundation of
819 China (No. T2122016, YM), and an International Postdoctoral Exchange Fellowship Program (No.
820 PC2021005, ZJ).

821 **Author Contributions:** TC, ZJ and SW conceptualized and designed the research. TC, ZJ, JZ, and YM
822 analyzed the model and performed the simulations. ZJ, WZ, TH, NB and SW interpreted the results.
823 ZJ, TC, DB, NB and SW wrote the manuscript.

824 **Competing interests:** Authors declare that they have no competing interests.

825 **Data and materials availability:** All code for reproducing the figures in the main text are available
826 in the supplementary materials.

827 **List of material contained in the Supplementary Material**

- 828 • Supplementary text (pdf file)
- 829 • Figures S1-S4
- 830 • Video 1-4
- 831 • Code for reproducing all the figures in the main text